Title:

Electrochemical reduction behavior of vitrified nuclear waste simulant in molten $CaCl_2$

Authors:

Yumi KATASHO,[a, b, *] Kouji YASUDA,[c, d, 1] Tetsuo OISHI[b], Toshiyuki NOHIRA[a,*]

Affiliation:

[a]Institute of Advanced Energy, Kyoto University, Gokasho, Uji, Kyoto 611-0011, Japan.

[b]Global Zero Emission Research Center, National Institute of Advanced Industrial Science and Technology (AIST), 16-1 Onogawa, Tsukuba 305-8569, Japan

[c]Agency for Health, Safety and Environment, Kyoto University, Yoshida-honmachi, Sakyo-ku, Kyoto 606-8501, Japan.

[d]Department of Fundamental Energy Science, Graduate School of Energy Science, Kyoto University, Yoshida-honmachi, Sakyo-ku, Kyoto 606-8501, Japan.

1. Present address: Department of Materials Science and Engineering, Graduate School of Engineering, Kyoto University, Yoshida-honmachi, Sakyo-ku, Kyoto 606-8501, Japan.

[*]Corresponding Authors:

katasho.yumi@aist.go.jp (Y. Katasho)

nohira.toshiyuki.8r@kyoto-u.ac.jp (T. Nohira)

Tel.: +81-774-38-3500; Fax: +81-774-38-3499.

Highlights

- Vitrified waste simulant including LLFP elements was electrolyzed in molten $CaCl_2$
- The simulant was electrochemically reduced to form Si, CaB_6, and REB_6
- $E-pO^{2-}$ diagrams were constructed to predict the behaviors of constituent elements
- The behaviors of most of the elements during the electrolysis were clarified

Abstract

The electrochemical reduction of vitrified nuclear waste simulant glass produced by melting oxides of 33 different elements, including Si and four types of long-lived fission product elements (Cs, Zr, Pd, and Se), was investigated in molten $CaCl_2$ at 1103 K. Before the experiment, potential−pO^{2-} diagrams were constructed from the thermodynamic data to predict the behaviors of the constituent elements during the electrochemical reduction. In the first experiment, small crucible electrodes containing approximately 100 mg of the simulant were electrolyzed at 0.6–1.1 V vs. Ca^{2+}/Ca. X-ray diffraction analysis confirmed that SiO_2 was reduced to Si. In addition, the formation of XB_6 (X = Ca, Si, or rare earth elements (REEs)) was confirmed. In the second experiment, a large crucible electrode containing approximately 10 g of the simulant was galvanostatically reduced at −2 A for 5 h. The distribution ratios of the constituent elements to the solid product and to the molten salt were calculated from the result of composition analysis using inductively coupled plasma atomic emission spectrometry and mass spectrometry. In particular, four types of long-lived fission product elements (Cs, Zr, Pd, and Se) were investigated. Consequently, alkali and alkaline earth elements, including Cs, were dissolved into the molten salt. Si mostly remained in the solid product as elemental silicon. Most of the other elements, including Zr and Pd, were also found in the solid product. Se and Zn were indicated to partially evaporate depending on the duration of electrolysis.

Keywords:

Molten salt; vitrified radioactive waste; electrochemical reduction; potential−pO^{2-} diagram

1. Introduction

Nuclear power generation has increased significantly in recent decades. The number of nuclear power plants is expected to rapidly increase in the future owing to the growing population, rising energy demands, and diminishing fossil fuel supplies. However, nuclear power generation involves the critical issue of radioactive waste disposal. The amount of radioactive waste is expected to increase with the increase in nuclear power generation. Moreover, site determination for the geological disposal of radioactive waste is difficult, especially in Japan, because of catastrophic geological events such as volcanic eruptions and earthquakes.

On the other hand, technologies for decreasing the amount of radioactive waste have been investigated in Japan since the 1980s under the OMEGA program [1]. Recently, another program, namely the ImPACT program [2], was launched with the same objective. In the first step of this program, long-lived fission products (LLFPs), such as ^{135}Cs, ^{79}Se, ^{93}Zr, and ^{107}Pd, are separately recovered from the high-level radioactive waste (HLWs) and also from the vitrified radioactive waste produced previously. In the next step, they are converted into short-lived or stable nuclides by nuclear transmutation. The nuclear transmutation reaction experiments of ^{107}Pd [3] and ^{135}Cs [4] have already commenced. The realization of this process facilitates a significant reduction in the amount of HLWs and vitrified waste, because the waste containing no LLFPs can be disposed as stable waste. Moreover, some elements, including precious metals such as Pd, can be salvaged.

The recovery of LLFPs from the vitrified waste requires the decomposition of the Si–O network structure of the glass in the initial step. Recently, we proposed electrochemical reduction in molten $CaCl_2$ for the decomposition of the glass network structure [5–7]:

$$SiO_2 + 4\ e^- \rightarrow Si + 2\ O^{2-}\ (\text{in molten } CaCl_2) \quad (1)$$

The details of this molten salt electrolysis process have been presented in our previous paper [7]. Realizing the new disposal process requires clarification of the behavior of the constituent elements, including LLFPs, during the electrolysis of the vitrified waste in molten $CaCl_2$.

In our previous studies, electrochemical reduction of borosilicate glass and two types of simplified simulants of vitrified radioactive waste was investigated [5–7]. Their compositions are summarized in Table 1. In the electrochemical reduction of borosilicate glass, the main component, SiO_2, was reduced to crystalline Si by potentiostatic electrolysis at 0.9 V vs. Ca^{2+}/Ca in molten $CaCl_2$ at 1123 K [5,6]. In addition, the reduction of B_2O_3 and dissolution of Na_2O were indicated [5,6]. The behaviors of the constituent elements, i.e., Si, B, Al, Na, and K, were in agreement with the potential–pO^{2-} diagrams constructed from the thermodynamic data [6]. In the subsequent study, the electrochemical reduction of two types of simplified simulants of vitrified radioactive waste, simulant 1 (glass component only: SiO_2, B_2O_3, Na_2O, Al_2O_3, CaO, Li_2O, and ZnO) and simulant 2 (glass component and LLFP oxides, i.e., ZrO_2, Cs_2O, PdO, and SeO_2), was investigated in molten $CaCl_2$ at 1103 K [7]. The dissolution of Na, Li, and Cs from the simulants into molten $CaCl_2$ was confirmed. Most of the SiO_2 in the simulants was reduced to Si after electrolysis at 0.9 V vs. Ca^{2+}/Ca. In the case of simulant 2, Al, Zr, and Pd remained in the solid phase while SeO_2 was found to remain partially in the solid phase and partially evaporate.

In the present study, glass with nearly the same composition as real vitrified waste was prepared, which is hereafter referred to as simulant 3. Table 1 summarizes the

compositions of simulant 3 and other materials used in our previous studies [5-7]. Compared to simulant 2, many fission product elements, including a variety of rare earth elements, were added to simulant 3. Before the experiment, potential–pO^{2-} diagrams were constructed to predict the behaviors of the constituent elements during the electrochemical reduction. Then, two experiments were conducted as follows: simulant 3 was electrochemically reduced in molten $CaCl_2$ with a small crucible electrode in experiment 1 (Exp. 1) and with a large crucible electrode in experiment 2 (Exp. 2). The reduction products were analyzed via field emission scanning electron microscopy (FE-SEM), energy-dispersive X-ray spectroscopy (EDX), X-ray diffraction (XRD), inductively coupled plasma atomic emission spectrometry (ICP-AES), and mass spectrometry (ICP-MS). In addition, sampled molten salts were analyzed via ICP-AES and -MS.

2. Experimental procedure

2.1. Exp. 1 (small crucible)

Simulant 3 was prepared at IHI Co., Ltd., by melting the oxides of 33 different elements at the ratios listed in Table 2. To avoid radioactivity, simulant 3 was prepared using only stable isotopes and by replacing uranium with cerium.

Fig. 1a shows a schematic of the experimental apparatus for Exp. 1. Here, 450 g of $CaCl_2$ (>99%; Kojundo Chemical Laboratory Co., Ltd.) was put in an alumina crucible (outer diameter, 90 mm; height, 140 mm; purity, 99%; AS ONE Corp.) in an open dry chamber (HRW-60AR, Daikin Co., Ltd.). The crucible containing $CaCl_2$ was dried at 453 K in a vacuum oven for more than 72 h and then placed in a quartz glass vessel under vacuum at 773 K for 24 h to further remove the moisture. The experiments were conducted inside the quartz glass vessel at 1103 K in a dry Ar atmosphere. The

temperature was controlled using a thermostat connected to a chromel–alumel thermocouple installed in a vertical furnace, and the temperature of the molten salt was measured using another thermocouple immersed in the molten salt.

Electrochemical measurements and potentiostatic electrolysis were conducted via a three-electrode method using an electrochemical measurement system (HZ-3000, Hokuto Denko Corp.). The counter electrode was a graphite square rod (4 mm × 4 mm × 50 mm; IG-110, Toyo Tanso Co., Ltd.). The reference electrode was a Ag^{+}/Ag electrode prepared by immersing a silver wire (diameter, 1.0 mm; 99%; Nilaco Corp.) in a $CaCl_2$ melt containing 0.5 mol% AgCl (99.5%; Wako Pure Chemical Co., Ltd.) in a mullite tube (outer diameter, 6 mm; inner diameter, 4 mm; SiO_2, 40%; Al_2O_3, 56%; Nikkato Corp.) [8]. The potentials were calibrated by the Ca deposition/dissolution potential（Ca^{2+}/Ca）measured using a Mo electrode [8].

For electrochemical measurements, the glass-seal electrode was prepared using the same method as that in the previous study on simulant 1 [7]. Stainless steel SS 430 (diameter, 1.2 mm; coefficient of linear thermal expansion, $104 \times 10^{-7}\ K^{-1}$; composition, C < 0.12 wt%, Si < 0.75 wt%, Mn < 1.00 wt%, P < 0.04 wt%, S < 0.03 wt%, Cr 16.00–18.00 wt%; Nippon Seisen Co., Ltd.) was selected as the metal rod material because its thermal expansion coefficient is similar to that of simulant 3. The stainless steel rod was dipped in the melted simulant 3 under an Ar atmosphere at 1123 K [7]. After cooling to ambient temperature, the stainless steel rod sealed with simulant 3 was vertically cut using a desktop abrasive cutting machine (RC-120, AS ONE Corp.) and polished using emery paper to prepare the three-phase interface of simulant 3/$CaCl_2$/conductor (stainless steel or reduced Si) on the bottom and side. In the cyclic voltammetry, the measurement was commenced immediately after the immersion of the electrode in molten $CaCl_2$ to prevent deformation of the glass.

The small crucible electrode shown in Fig. 1b was used for potentiostatic electrolysis [7,9]. This electrode was prepared by cutting an Al_2O_3 tube (outer diameter, 8 mm; inner diameter, 5 mm; height, 10 mm; 99.6%; Nikkato Corp.) and inserting a graphite plate (10 mm × 10 mm × 0.5 mm; 99.5%; Nilaco Corp.). A Ni wire (diameter, 1.0 mm; 99%; Nilaco Corp.) was used as the current lead and connected to the carbon plate by threading it into a drilled hole (diameter, 1.0 mm). Two Ni wires (diameter, 0.5 mm; 99%; Nilaco Corp.) were wound around the Al_2O_3 tube to fix the Ni lead wire. The pellet (diameter, 5 mm) was prepared in the same manner as that in the case of simulant 2 [7]. Specifically, simulant 3 and $CaCl_2$ were crushed and the particles smaller than 0.2 mm were mixed in the open dry chamber. The weights of simulant 3 and $CaCl_2$ were approximately 100 mg and 40 mg, respectively. The pellet was prepared at approximately 0.3 MPa and placed inside the small crucible electrode. The Ni lead wire of the small crucible electrode was finally spot-welded to a Mo lead wire (diameter, 1.0 mm; 99.95%; Nilaco Corp.). Using this small crucible electrode, potentiostatic electrolysis was carried out for 1 h at several potentials. For comparison, a sample only immersed in the melt for 1 h was also prepared.

After the potentiostatic electrolysis, the samples were taken out from the molten salt and rinsed with distilled water to remove the solidified salts. Then, they were cut using the desktop abrasive cutting machine. Their cross section was observed using an optical digital microscope (Dino Lite PRO Polarizer DILITE30 AM-413ZT, Sanko Co., Ltd.). Subsequently, the samples were soaked in 3 mol/L HCl solution for more than 8 h to remove the residual salt and calcium silicates formed during the electrolysis. Then, the remaining solid was recovered from the solution by suction filtration, dried at 353 K, and analyzed via XRD (Cu–Kα line; Ultima IV, Rigaku Corp.). The remaining solid was also observed via FE-SEM (JSM-6500FE, JEOL Co., Ltd.),

To evaluate the distribution of elements in the solid product and molten salt, the equal number of abovementioned immersion and potentiostatic electrolysis at 0.6 V were carried out in a new identical $CaCl_2$ melt. For this evaluation via ICP-AES and -MS, the samples were not cut after the immersion or electrolysis. From the solid products, the residual salt was dissolved using distilled water, and the Ni wires were removed. Two different methods were adopted to dissolve the solid products. In the first method, the samples were dissolved in 3 mol/L HCl solution agitated using a magnetic stirrer for 48 h. The solid and liquid phases were separated by suction filtration. The solid phase was further dissolved into a mixture of concentrated $HF+HNO_3$ (HF, 38 wt%; HNO_3, 68 wt%; volume ratio, 1:1.4) for 24 h. The $HF+HNO_3$ solution was separated from the residue by suction filtration, and ultrapure water was then added to obtain a total volume of 100 mL. In the second method, the samples were dissolved into a mixture of concentrated HNO_3+HCl+HF (68%, 35%−37%, 38%; volume ratio, 1:1:1) using a microwave decomposition machine (ETHOS One, Milestone Co., Ltd) at 503 K. The solutions thus obtained were analyzed via ICP-AES (SPECTRO Blue, Hitachi High-Tech Science Corp.) and ICP-MS (7700x, Agilent Technologies, Inc.).

A part of the molten salts was sampled via the suction method using a mullite tube (outer diameter, 5 mm; inner diameter, 3 mm; Nikkato Corp.) and a pipet bulb immediately after the immersion and electrolysis experiments. The solidified salt collected in the tube was weighed in the open dry chamber. Approximately 3 g of the collected salt was dissolved in 100 mL of 1 mol/L HNO_3 solution and analyzed via ICP-AES and -MS.

2.2. Exp. 2 (large crucible)

Fig. 2 shows a schematic of the experimental apparatus for Exp. 2. The weight ratio of $CaCl_2$ to simulant 3 was approximately 20. First, 200 g of $CaCl_2$ (>99%, Kojundo Chemical Laboratory Co., Ltd.) was put in a graphite crucible (inner diameter, 80 mm; height, 150 mm; Toyo Tanso Co., Ltd.) in the open dry chamber. A graphite rod was connected to the crucible with carbon bolts and nuts. The experiment was conducted inside the quartz glass vessel at 1103 K in a dry Ar atmosphere. Many pellets were fabricated similarly to Exp. 1. The total weights of simulant 3 and $CaCl_2$ in the pellets were approximately 10 g and 4 g, respectively. After increasing the temperature of the melt, all the pellets were put into the melt.

Galvanostatic electrolysis was conducted via a three-electrode method using an electrochemical measurement system (HZ-7000, Hokuto Denko Corp.). The counter and reference electrodes were the same as those used in Exp. 1. Molten salts before and after the electrolysis were sampled, and their compositions were analyzed via ICP-AES and -MS. In Exp. 2, the amounts of the initial impurities in the molten salts were subtracted in the evaluation. The reduction products were collected after removing $CaCl_2$ with distilled water at 353 K on a hot plate. After suction filtration and drying at room temperature, the collected products were weighed. The products contained white cylindrical lumps, which were regarded as unreacted simulant 3 and removed using tweezers, and the remaining black powder was analyzed. A part of the black powder was further rinsed in 3 mol/L HCl solution and dried on the hot plate before XRD analysis. The remaining black powder was dissolved for measurement via ICP-AES and -MS using three different methods. In the first method, microwave dissolution was conducted twice. The sample was dissolved into a mixture of concentrated HNO_3+HCl (68%, 35%–37%; volume ratio, 1:3) at 503 K via microwave dissolution, and the residue separated from the liquid phase by filtration was further dissolved into a mixture

of concentrated HNO_3+HCl+HF (68%, 35%–37%, 38%; volume ratio, 1:1:1) at 503 K via microwave dissolution. The other two methods were the same as those in Exp. 1, i.e., sequential dissolution in 3 mol/L HCl solution and a mixture of concentrated HNO_3+HF, and one-step dissolution in a mixture of concentrated HNO_3+HCl+HF. These solutions were analyzed via ICP-AES and -MS. The distributions of the constituent elements were calculated from the weight of the analyzed sample and the results of ICP-AES and -MS. Among the three dissolution methods, the method that gave the closest value to unity for the sum of the distribution ratios in the solid reduced product and the molten salt was chosen for each element, because the optimal dissolution method depends on the element.

3. Thermodynamic calculations

The thermochemical data used in the present study are summarized in Table 3 [8,10−46]. Most of the thermochemical data were taken from HSC Chemistry 9.8.1.2 (Outotec) [47]. Here, the standard states are pure solid, pure liquid, and gas with atmospheric pressure for the stable states at 1123 K.

3.1. Plot of the standard Gibbs energy of formation of oxides and chlorides

As the first step of thermodynamic calculation, the dissolution behavior of the constituent oxides in molten $CaCl_2$ was investigated. Fig. 3 plots the standard Gibbs energies of formation of oxides on the vertical axis and those of chlorides on the horizontal axis. The oxides/chlorides are plotted using the values marked with an asterisk in Table 3. The plot for Se cannot be obtained because of the lack of thermodynamic data at the same valency. The standard Gibbs energies of formation of $CaCl_2$ is represented by the vertical black dashed line.

Assuming that all the chlorides dissolve into molten $CaCl_2$, the dissolution behavior of the constituent oxides can be roughly evaluated based on reaction (2). Note that the value for CaO(*s*) is used here for simplification and that for CaO(*l*) is used for a more detailed discussion in Section 3.2.

$$\frac{1}{x}\,MO_x(s, l, or\ g) + CaCl_2(l) \rightarrow \frac{1}{x}\,MCl_{2x}(s, l, or\ g) + CaO(s) \quad (2)$$

The difference of the standard Gibbs energy of reaction (2), $\Delta G^{\circ}_{(Dis\_CaCl_2)}$, is calculated as

$$\Delta G^{\circ}_{(Dis\_CaCl_2)} = \left(\frac{1}{x}\Delta G_f^{\circ}(MCl_{2x}) + \Delta G_f^{\circ}(CaO)\right) - \left(\frac{1}{x}\Delta G_f^{\circ}(MO_x) + \Delta G_f^{\circ}(CaCl_2)\right) \quad (3)$$

The orange line in Fig. 3 corresponds to the zero value of $\Delta G^{\circ}_{(Dis\_CaCl_2)}$. The elements in the yellow region (Rb, Cs, Na, Li, Ba, Ag, and Sr) are supposed to be dissolved into molten $CaCl_2$ owing to the negative value of $\Delta G^{\circ}_{(Dis\_CaCl_2)}$.

The horizontal blue dashed line represents the standard Gibbs energy of formation of SiO_2. The elements whose oxides are reduced at a more positive potential than that of SiO_2 are plotted above this line. Conversely, the elements below the line are those whose oxides are reduced at a more negative potential than that of SiO_2. Since Ag_2O has a positive standard Gibbs energy of formation, Ag_2O is unstable at 1123 K. It will decompose into metallic Ag and O_2 gas. Several elements in the blue region (Se, Zn, Mn, La, Pr, and Ce) close to the orange line might partially dissolve into the molten salt.

Other elements located well below the orange line will not dissolve when they are only immersed in molten $CaCl_2$.

Investigating the behavior of each element precisely requires each phase diagram of MCl_{2x}–$CaCl_2$ or the solubility of MO_x in $CaCl_2$ to be checked. In addition, the behavior of the elements at each activity of CaO needs to be investigated, as discussed in the following section.

3.2. Potential–pO^{2-} diagrams

To predict the behaviors of the constituent elements of simulant 3, the potential–pO^{2-} diagrams for various M in molten $CaCl_2$ at 1123 K were constructed, where M = Si, B, Na, Al, Li, Zn, Zr, Cs, Pd, Se, U, Rb, Sr, Ba, Y, La, Ce, Pr, Nd, Sm, Eu, Gd, Ru, Rh, Ag, P, Sn, Te, Cr, Mn, Fe, Ni, and Mo. The systems for Si, B, Na, Al, Li, Zn, Zr, Cs, Pd, and Se are revised owing to the recent update of the thermodynamic data [47], although they have already been reported in our previous papers [6,7]. The construction method of the diagrams has also been described in those papers. As a precondition for this calculation, all the chlorides and $UO_2Cl_2(l)$ are assumed to be dissolved and exist as ions in molten $CaCl_2$ having an activity of 10^{-2}, while the activities of the other species except for O^{2-} are fixed at unity. $UO_2Cl_2(l)$ is reported to be dissolved as UO_2^{2+} ions in LiCl–KCl melts [48], while most oxychlorides are insoluble in chloride melts. Thus, $UO_2Cl_2(l)$ was also regarded as a soluble substance in the present study. The expression for ions, not chloride compounds, is used because most of these elements' chlorides are considered to be certainly dissolved into $CaCl_2$ from the phase diagrams. This assumption is much closer to real chemical behavior in molten $CaCl_2$ than that expressed by chloride compounds.

To construct the potential–pO^{2-} diagrams, the Ca^{2+} ion and the equilibrium potential for $Ca^{2+}/Ca(l)$ were selected as the standard ion and standard potential, respectively. The chemical potential of CaO(*l*), which represents dissolved CaO in molten $CaCl_2$, was determined by the solubility of CaO(*s*) in molten $CaCl_2$ at 1123 K similarly to other published potential–pO^{2-} diagrams [6–8]. The evolution potential of 1 atm O_2 gas changes with the pO^{2-} value as follows [6–8]:

$$E_{O_2/O^{2-}} = 2.575 + 0.111\ pO^{2-} \quad (4)$$

3.2.1 Main components and LLFP elements (M = Si, B, Na, Al, Li, Zn, Zr, Cs, Pd, and Se)

Fig. 4a–j shows the potential–pO^{2-} diagram for Si, B, Na, Al, Li, Zn, Zr, Cs, Pd, and Se, respectively, in molten $CaCl_2$ at 1123 K. These are basically the same as those reported previously [6,7], although some boundaries are slightly shifted owing to the update of the thermodynamic data. The main changes are in the enlarged region of the dissolved species, because their activities are defined as 10^{-2} in the present study. Although 1123 K is above the boiling point of $ZnCl_2$, $ZnCl_2(l)$ appears in the diagram because $ZnCl_2(l)$ with an activity of 0.01 is more stable than $ZnCl_2(g)$ at 1 atm. Other updates are the additional calculation in the virtual regions, such as more positive potential than Cl_2 or O_2 gas evolution and the region $pO^{2-} < 0.954$ (lower than the value corresponding to the solubility of CaO).

3.2.2 Uranium (M = U)

Thus far, the potential–pO^{2-} diagrams for U in LiCl–KCl at 723 K have been reported by Uchida *et al.* [48] and Brown *et al.* [49]. Recently, Abdulaziz *et al.* reported

the diagrams for U in both LiCl–KCl at 773 K and NaCl–KCl at 1023 K [50]. In addition, Brown *et al.* reported the diagram for U in $CaCl_2$ at 1073 K [51].

Fig. 5a shows the potential–pO^{2-} diagram for U in molten $CaCl_2$ at 1123 K. Although U is not present in simulant 3, the prediction of the electrochemical reduction behavior of UO_2 in molten $CaCl_2$ is important because the real vitrified waste contains U. Calcium uranate ($CaUO_4(s)$) appears in the low pO^{2-} region, and uranium oxychloride, i.e., $UO_2Cl_2(l)$, which is assumed to exist as UO_2^{2+}, appears in a more positive potential region than 2.8 V. The stable region for $UO_2(s)$ is located in a more negative region compared to $U_3O_8(s)$ and $U_4O_9(s)$. The chlorides $UCl_3(l)$ and $UCl_4(l)$ as U^{3+} and U^{4+}, respectively, are stable in the high pO^{2-} region and more positive potential region than 0.94 V. The present diagram is essentially the same as that reported by Brown *et al.* [51], except for the presence of the stable region of $U_4O_9(s)$. The difference is probably due to the difference in the assumptions and thermodynamic data used for the calculation.

3.2.3 Alkali and alkaline earth elements (M = Rb, Sr, and Ba)

Fig. 5b–d shows the potential–pO^{2-} diagrams for Rb, Sr, and Ba, respectively, in molten $CaCl_2$. The stable phases are only chlorides, which readily dissolve into molten $CaCl_2$ and are expressed as ions in the diagrams. Dissolution of the constituent oxides occurs when they are immersed in molten $CaCl_2$:

$$Rb_2O\ (s, \textit{in glass}) \rightarrow 2\ Rb^+ + O^{2-} \quad (5)$$

$$SrO\ (s, \textit{in glass}) \rightarrow Sr^{2+} + O^{2-} \quad (6)$$

$$BaO\ (s, \textit{in glass}) \rightarrow Ba^{2+} + O^{2-} \quad (7)$$

As the decomposition voltages of RbCl(*l*), $SrCl_2$(*s*), and $BaCl_2$(*l*) are larger than that of $CaCl_2$, metal deposition of Rb, Sr, and Ba does not occur in a more positive potential range than 0 V.

3.2.4 Rare earth elements (M = Y, La, Ce, Pr, Nd, Sm, Eu, and Gd)

Thus far, the potential–pO^{2-} diagrams for Ce in $CaCl_2$–NaCl at 823 K and in LiCl–KCl at 723 K have been reported by Castrillejo *et al.* [52]. Furthermore, Sakamura constructed the diagram for La in LiCl at 923 K [53]. In addition, potential–pO^{2-} diagrams for a variety of rare earth elements in LiCl–KCl have been extensively studied by many researchers [50, 54–56]. Abdulaziz *et al.* reported the diagrams for Nd, Sm, Eu, and Gd in both LiCl–KCl at 773 K and NaCl–KCl at 1023 K [50]. However, the potential–pO^{2-} diagrams for rare earth elements and their oxides in $CaCl_2$ at 1123 K have not been reported thus far.

Fig. 5e–l shows the potential–pO^{2-} diagrams for Y, La, Ce, Pr, Nd, Sm, Eu, and Gd, respectively, in molten $CaCl_2$. In all the diagrams, the chlorides shown as ions are stable in the high pO^{2-} region. The diagrams for Y, La, Ce, Pr, Nd, and Gd in molten $CaCl_2$ have a stable region of the metals at a negative potential. On the other hand, there is no stable region of metallic Sm and Eu in the potential region described in Fig. 5i and k owing to the high stability of divalent chlorides. The diagrams for La, Nd, Sm, Eu, and Gd have a stable region of oxychlorides. As for Ce and Pr, several types of oxides are stable in the corresponding diagrams.

As explained in the experimental section, uranium was replaced by cerium to avoid radioactivity. In the region of $pO^{2-} < 3.5$, which is the realistic pO^{2-} region for the experimental system, the reduction behaviors of Ce and U are similar. Specifically, both Ce and U are stable as oxides or $CaUO_4$ in a more positive potential region than

0.7 V, and they are reduced to metallic Ce or U at a more negative potential than 0.4 V and 0.7 V, respectively. Regardless of the applied potential, both Ce and U compounds are expected to stay in the solid product. However, there is a possibility of different behaviors of U and Ce, as there are differences in the stable phases and regions between the U and Ce systems in their diagrams.

3.2.5 Precious metal elements (M = Ru, Rh, and Ag)

Thus far, Abdulaziz *et al.* reported the potential–pO^{2-} diagrams for Ru, Rh, and Ag in both LiCl–KCl at 773 K and NaCl–KCl at 1023 K [50]. The potential–pO^{2-} diagrams including precious metals in $CaCl_2$ at 1123 K have not been reported thus far.

Fig. 5m–o shows the potential–pO^{2-} diagrams for Ru, Rh, and Ag, respectively, in molten $CaCl_2$. Metallic Ru and Rh have a large stable region. In the diagram for the Ru system, RuO_2(*s*) appears in the positive potential region close to the oxygen gas evolution. In the diagram for the Rh system, two oxides and one chloride shown as Rh^{3+} appear in the positive potential region. In the Ag system, the stable compounds are AgCl(*l*) as Ag^+ and Ag(*s*). The equilibrium potential between Ag^+ and Ag(*s*) is 2.01 V. The stable region of Ag_2O(*l*) does not appear because the Gibbs energy of formation for Ag_2O(*l*) is positive at this temperature.

3.2.6 Groups 14 to 16 (M = P, Sn, and Te)

Fig. 5p–r shows the potential–pO^{2-} diagrams for P, Sn and Te, respectively, in molten $CaCl_2$. In all three diagrams, Ca–M compounds and elemental states appear in the negative potential region. In the diagram for the P system, two types of Ca–P–O compounds are stable in the positive potential region. Elemental P is stable as the gas phase at this temperature. Oxychloride gas and two types of chloride gases are stable in

the high pO^{2-} and positive potential region. In the diagram for the Sn system, the metallic Sn region exists in the middle potential range. $SnO_2(s)$ and $SnCl_2O_2(g)$ are stable in the positive potential and low pO^{2-} region. Two types of chlorides are stable in the high pO^{2-} and positive potential region. In the diagram for the Te system, CaTe(*s*) and elemental Te(*l*) are stable at a more negative potential than 1.94 V. TeO(*l*) and $TeCl_2(g)$ appear in the positive potential region. In the negative potential region, CaTe may be dissolved into the melt as Te^{2-} ion. A detailed explanation for Te^{2-} ion is provided in Section 4.5.5.

3.2.7 Other transition elements (M = Cr, Mn, Fe, Ni, and Mo)

Thus far, Abdulaziz *et al.* [50] have reported the potential–pO^{2-} diagrams for Mo in both LiCl–KCl at 773 K and NaCl–KCl at 1023 K. The potential–pO^{2-} diagrams for Cr, Mn, Fe, Ni, and Mo and their oxides in $CaCl_2$ at 1123 K have not been reported thus far.

Fig. 5s–w shows the potential–pO^{2-} diagrams for Cr, Mn, Fe, Ni, and Mo, respectively, in molten $CaCl_2$. For all the systems, the stable regions of metals are located in a more negative potential region than 1 V. In the Cr system, three types of chlorides exist in the high pO^{2-} and positive potential region. Calcium chromate ($CaCr_2O_4(s)$) is stable in the low pO^{2-} and positive potential region. In the Mn system, a large stable region for $MnCl_2(l)$ as Mn^{2+} appears in the high pO^{2-} and positive potential region. Furthermore, five types of oxides are stable in the low pO^{2-} and positive potential region. In the diagram for Fe, two types of chlorides expressed as Fe^{2+} and Fe^{3+} ions are stable in the high pO^{2-} and positive potential region. Then, three types of oxides appear near the Fe^{2+} region. In the lowest pO^{2-} region, the stable region of calcium iron oxide ($CaFe_2O_4(s)$, $Ca_2Fe_2O_5(s)$) exists. In the Ni system, there exist three

stable regions of NiO(*s*), $NiCl_2$(*l*) as Ni^{2+}, and Ni(*s*). In the Mo system, two types of calcium molybdates ($CaMoO_3$(*s*) and $CaMoO_4$(*s*)) are stable in a relatively large region with low pO^{2-} and positive potential values. There are three stable regions for the oxide and oxychloride compounds, i.e., MoO_2(*s*), $MoCl_2O_2$(*g*), and $MoCl_3O$(*g*). Two types of chlorides as Mo^{3+} and Mo^{4+} are stable at a more positive potential than 2.37 V.

4. Experimental Results and Discussion

4.1. Cyclic voltammetry

Fig. 6a shows a schematic of the vertical cross section of the glass-seal electrode of simulant 3. The reaction proceeds at the three-phase interface among simulant 3, the conductor (stainless steel rod or reduced Si), and molten $CaCl_2$. In the present experiment, the reaction zone is located both on the side and on the bottom of the electrode, as shown in red in Fig. 6a.

Fig. 6b and c shows photographs of the electrode before and after the cyclic voltammetry. As with the behavior of simulant 1 [7], the color changed from no color to black owing to the formation of black reduction products.

Fig. 6d shows the cyclic voltammograms for five consecutive cycles measured using the glass-sealed electrode of simulant 3. The apparent current density is calculated from the area of the stainless steel rod in contact with the molten salt. As with the behavior of the glass-sealed electrode of SiO_2 [5], Pyrex [5], and simulant 1 [7], the current increases with the cycle number owing to the increase in the reaction zone as a result of the formation of conductive Si from insulating SiO_2. Furthermore, the shape of the voltammogram is similar to that for simulant 1 even though simulant 3 contains many types of metal oxides that were not included in simulant 1. In our previous study on simulant 1 [7], cathodic currents for the reduction of B_2O_3 and ZnO were observed

at 1.8 V, while that of SiO_2 was measured at 1.3 V. In addition, a sharp increase in the cathodic current for the formation of Si–Ca alloys was observed at 0.5 V. In the case of simulant 3, the cathodic current at 1.8 V is assumed to correspond to the reduction of oxides whose ΔG_f° (MO_x) is higher than ΔG_f° (SiO_2), such as the oxides of Mn, Cr, P, B, and Zn. The cathodic current observed at 1.3 V is believed to mainly correspond to the reduction of SiO_2. At a more negative potential than 0.6 V, oxides more stable than SiO_2, such as Al_2O_3, ZrO_2, and Nd_2O_3, may also be reduced. Here, the cathodic current at 0.3−0.4 V also largely includes the current attributed to the formation reaction of Si–Ca alloy. After reversing the scan direction at 0.3 V, the anodic current, which is believed to be due to the dissolution of Ca from the formed Si–Ca alloy, is observed at 0.5−0.8 V. The anodic currents observed at 1.0 V are thought to correspond to the oxidation of Si and other metals.

4.2. Analysis of the electrolyzed simulant 3 in Exp. 1

The pellet prepared from the mixture of simulant 3 and $CaCl_2$ powder was potentiostatically electrolyzed at different potentials. Fig. 7a shows cross-sectional micrographs of the small crucible electrodes electrolyzed at 1.4, 1.1, 1.0, 0.9, and 0.6 V for 1 h. For comparison, the sample was prepared by only immersion in molten salt for 1 h. No color change was observed in the case of immersion. At 1.4 V, a part of the pellet became brown, which indicates the reduction of oxides. A similar color change to brown was observed for half of the pellet at 1.1 V. For the samples at 1.0, 0.9, and 0.6 V, the entire pellet became brown.

In the current–time curves shown in Fig. 7b, nearly constant currents are observed at 1.4 V and 1.1 V, because the reduction is not completed at the end of the electrolysis. At 1.0, 0.9, and 0.6 V, the current shows peaks at 20−40 min, corresponding to

situations in which the reaction area of the three-phase interface increases and the reduction reaction proceeds toward completion. In particular, the current at 0.6 V rapidly decreases to approximately −50 mA after 30 min, which indicates the completion of the reduction of the entire pellet.

Fig. 7c shows cross sections of the small crucible electrodes after electrolysis at 0.6 V for 5, 10, 20, and 30 min. The reacted area grew from the bottom conductor as the electrolysis time increased. The effective reduction rate was nearly twice as high as that of simulant 2, although the electrolytic condition and procedure to prepare the simulant–$CaCl_2$ pellets were the same as those in our previous study [7]. Some elements existing in their metallic states in the glass, such as platinum-group metals (see the potential–pO^{2-} diagrams for Ru, Rh, and Ag shown in Fig. 5m–o, respectively), might contribute to the acceleration of the reduction reaction because the presence of these metals can increase the electrical conductivity of the reduction products and unreacted glass.

Fig. 8a shows the XRD patterns of simulant 3 samples after being washed with 3 mol/L HCl solution. For the samples electrolyzed at a more negative potential than 1.1 V, the peaks attributed to Si were confirmed. The reduction of the main component of SiO_2 to Si is consistent with the color change observed in the cross-sectional images shown in Fig. 7a. The immersion sample and the reduced samples at 1.4, 1.1, and 1.0 V had peaks assigned to α-quartz. Since α-quartz was not detected from simulant 3, it was formed during the immersion in molten $CaCl_2$ similarly to the samples of simulants 1 and 2 [7]. The pattern of $Zr_{0.9}Ce_{0.1}O_2$ was detected from all the samples except for 0.6 V. XRD peaks from the immersion sample and the reduced sample at 1.4 V coincided well with the reference pattern of metallic Ru. The pattern of Ru_2Si_3 was detected from the samples at 1.1 V or more negative potentials. Although further investigation is

required because of the low concentration of RuO_2 in simulant 3, i.e., 0.70 wt%, we attribute these peaks to metallic Ru and Ru_2Si_3 at present. The formation of metallic Ru at a positive potential of 1.4 V is reasonable because of the large stable region of metallic Ru in the potential–pO^{2-} diagram for the Ru system (Fig. 5m). Ru_2Si_3 was produced at a more negative potential of 1.1 V. The potential–pO^{2-} diagram for the Si system (Fig. 4a) shows that SiO_2 or calcium silicate can be reduced to Si at 1.1 V, pO^{2-} > 3.98, which is possible in the laboratory experiment, especially at the beginning of the electrolysis. From the potential–pO^{2-} diagram for the Ru system (Fig. 5m), metallic Ru is also stable at this potential. Thus, the formation of Ru_2Si_3 at a more negative potential than 1.1 V is reasonable because both elemental Si and Ru are stable in this condition and the Ru_2Si_3 phase exists in the Ru–Si phase diagram [57]. The formation of XB_6 (X = Ca, Si, or rare earth elements (REEs)) was confirmed at a more negative potential than 1.1 V. The peak patterns for XB_6 (X = Ca, Si, or REEs) are nearly identical as shown in Fig. 8b, because of their similar structure and lattice size. Thus, each XB_6 compound could not be identified straightforwardly. The reduction products probably contained REB_6 (rare-earth hexaboride) because the relatively strong XRD peak at 2θ = 21.4° is characteristic of REB_6, which is quite weak in the cases of CaB_6 and SiB_6 (Fig. 8b). The formation of REB_6 cannot be explained only by the potential–pO^{2-} diagrams, because REB_6 was not taken into consideration in constructing the potential–pO^{2-} diagrams. Therefore, additional calculation is performed in the next paragraph. Moreover, the reduction products at 0.9 and 0.6 V probably contained CaB_6, because we already confirmed its formation in the reduction products of simulant 2 at 0.9 and 0.6 V [7], whose main components are the same as those of simulant 3. The formation of CaB_6 is not consistent with the thermodynamic calculation shown in Fig. 4b. This discrepancy has already been reported in papers on the electrochemical

reduction of simulants 1 and 2 [7] and CaB_2O_4 [58]. The formation of SiB_6 is also possible at a more negative potential than 0.9 V. To distinguish CaB_6 and SiB_6, further investigation is required.

The formation of REB_6 was thermodynamically analyzed. Elemental B is stable in a potential range more negative than 1.1 V when $pO^{2-} > 3.52$, as shown in Fig. 4b. Under this condition, the formation of REB_6 can be explained in the following reaction, where RE^{3+} denotes a trivalent rare-earth ion.

$$RE^{3+} + 6\,B(s) + 3\,e^- \rightarrow REB_6(s) \tag{8}$$

As REB_6 and elemental B equilibrate according to the phase diagrams for REEs–B systems, the standard formation potential of REB_6 in reference to the standard redox potential for RE^{3+}/RE was calculated from the standard Gibbs energy of formation of REB_6, $\Delta G_f^\circ(REB_6)$.

$$E^\circ\left(RE^{3+},\ B/REB_6 \text{ vs. } RE^{3+}/RE\right) = -\frac{\Delta G_f^\circ(REB_6)}{3F} \tag{9}$$

Then, the formation potential of REB_6 with respect to the Ca^{2+}/Ca potential, $E^\circ(RE^{3+}, B/REB_6$ vs. $Ca^{2+}/Ca)$, was obtained from the standard redox potential of RE^{3+}/RE.

$$E^\circ(RE^{3+},\ B/REB_6 \text{ vs. } Ca^{2+}/Ca) = E^\circ(RE^{3+},\ B/REB_6 \text{ vs. } RE^{3+}/RE) + E^\circ(RE^{3+}/RE \text{ vs. } Ca^{2+}/Ca) \tag{10}$$

Table 4 summarizes our evaluation of the formation potential of REB_6 based on the above discussion. While the standard Gibbs energy of formation of REB_6 (RE = Ce, Gd, Nd, La, and Sm) at 1123 K [11, 13, 59−61] has been reported, thermodynamic data for PrB_6 and YB_6 are not available. As shown in the table, CeB_6, GdB_6, NdB_6, LaB_6, and SmB_6 can exist in the reduction products at a more negative potential than 1.46, 0.92, 0.98, 0.62, and 0.49 V, respectively. However, other formation potentials of REB_6 cannot be predicted.

In previous experimental research, electrochemical syntheses of hexaborides such as LaB_6 [62], CeB_6 [63], NdB_6 [64], EuB_6 [64], and GdB_6 [65] in chloride, chloride–fluoride, or fluoride melt have been reported. Although their experimental systems and conditions were not the same as those of our experiment, these studies have shown that the formation of REB_6 in molten salt is a natural result.

Simulant 3 reduced at 0.6 V for 1 h was observed via FE-SEM after being washed with 3 mol/L HCl solution. As shown in Fig. 9, a wire structure with a diameter of 300 nm was observed, especially on the upper side of the pellet. The morphology of the reduced sample was the same as that reported previously, in which the electrochemical reduction of SiO_2 to Si was confirmed in molten $CaCl_2$ [66–68]. EDX analysis of the same sample showed 67 at% Si, 22 at% O, 2 at% Ca, 5 at% Cl, and 2 at% Na, while the concentration of O in simulant 3 was 59 at%. If all the O present in SiO_2 is removed from simulant 3 by the electrolysis, the remaining O content is calculated to be 29 at%. Thus, most of the SiO_2 in simulant 3 is assumed to be reduced to Si. The remaining 22 at% of O is attributable to the oxides that cannot be reduced at 0.6 V.

4.3. Analysis of the electrolyzed simulant 3 in Exp. 2

Mass-scale electrochemical reduction is important to industrialize the proposed process. For the reduction of a large amount of simulant 3, we opted for a galvanostatic electrolysis process to control the reaction rate and prevent large currents in the initial stage of the electrolysis. The potential transient during the galvanostatic electrolysis at −2 A for 5 h is shown in Fig. 10a. After the initial drastic change, the potential gradually changed from 0.7 V to 0.5 V. The total electric charge was 36000 C, which corresponds to 114% of the theoretical quantity for the reduction of only the SiO_2 components in simulant 3.

Fig. 10b shows a photograph of the reduction products obtained by the electrolysis of 9.77 g of simulant 3. Sample (A) is a black powder weighing 16.24 g, and (B) is a coagulum of the unreduced pellets and reduced powder weighing 6.00 g. The increase in weight is attributable to the formation of $CaSiO_3$, $CaAl_{12}O_{19}$, and rare-earth oxychlorides, and to the reaction between the sample and water during the washing step.

The reduction products in Sample (A) were characterized via XRD after being washed with 3 mol/L HCl solution. Si and Ru_2Si_3 were detected as shown in Fig. 10c. The difference between the reduction products in Exp. 1 (Fig. 8a) and 2 (Fig. 10c) may be attributed to the difference in the pO^{2-} values. The ratio of $CaCl_2$ to simulant 3 was approximately 500 and 20 in Exp. 1 and Exp. 2, respectively. Assuming that simulant 3 is completely reduced, the minimum values of pO^{2-} are 2.50 and 1.14 in Exp. 1 and Exp. 2, respectively. Practically, the pO^{2-} value exceeds these values owing to the consumption of O^{2-} ions at the graphite anode to form CO or CO_2 gas and the incomplete reduction of all the oxides. $Al_{1.77}Ca_{0.88}O_8Si_{2.23}$ was identified from the reduction products in Exp. 2, while it was not found in Exp. 1. Although the formation of $Al_{1.77}Ca_{0.88}O_8Si_{2.23}$ cannot be predicted only by the potential−pO^{2-} diagrams, the Al−Ca−O and Si−Ca−O compounds are stable even in a relatively negative potential

region in the potential−pO^{2-} diagrams for Al and Si systems (Fig. 4a and 4c) at pO^{2-} = 1.14. Therefore, this increased stability of the Al−Ca−O and Si−Ca−O compounds may be the reason for the formation of $Al_{1.77}Ca_{0.88}O_8Si_{2.23}$ in Exp. 2. On the other hand, XRD peaks coinciding with XB_6 (X = Ca, Si, or REEs) were not measured from the reduction products in Exp. 2. This is explained by the negative shift of the boundary between calcium borate and elemental boron with a decrease in the pO^{2-} value from 2.50 in Exp. 1 to 1.14 in Exp. 2, as shown in the potential−pO^{2-} diagram for the B system (Fig. 4b). In addition, the boundary between the RE oxide or oxychloride and the RE metal shifted toward the negative direction according to the decrease in pO^{2-}. These are probably the reasons for the absence of XB_6 (X = Ca, Si, or REEs) in Exp. 2.

4.4. Behaviors of the constituent elements during immersion and electrolysis

Table 5 summarizes the element distribution for the solid phase and the molten salt in Exp. 1 and Exp. 2, which was standardized by the amounts of elements in simulant 3 used in these experiments. Note that the data for molten salt in Exp. 1 were influenced by both the immersion and electrolysis experiments because the molten salt was sampled after the completion of all the experiments in the same melt. The behavior of Sr can be investigated only in Exp. 2, because $CaCl_2$ used as the electrolytic bath contained 0.008 wt% Sr as an impurity, and the relative influence due to the impurity was large in Exp. 1. An analysis for P was not conducted owing to the difficulties in the analysis via ICP-AES and -MS.

First, the dissolution behaviors were analyzed from the comparisons between the immersed and reduced samples obtained in Exp. 1. In the case of B, 55% of B remained in the solid phase after immersion, while more than 80% of B remained when simulant 3 was electrolyzed. This difference can be explained as follows: (a) approximately a

half of B_2O_3 was dissolved into the molten salt when it was immersed for 1 h, and (b) most of B_2O_3 was reduced to form XB_6 (X = Ca, Si, or REE) as shown in Fig. 8a, when simulant 3 was electrolyzed. Concerning Zn, Mo, Mn, Te, Ni, and Se, they partially dissolved into the molten salt or evaporated from the system during the immersion, because their chlorides and oxides are stable as either gases or liquids at much more positive potentials than 0.6 V. Their ratios in the solid phase increased during electrolysis because their elemental form or calcium compounds were stable in their solid states at 0.6 V. The dissolution of Cs from simulant 3 during immersion seemed slower than that of the other alkali metals. When simulant 3 was electrolyzed at 0.6 V, the dissolution was facilitated after the decomposition of the Si−O network structure. The small value of Ru in the solid products was probably due to precipitation during the preparation of the aqueous solution for analysis via ICP-AES and -MS. The retention of Ru in the solid state in the cases of both immersion and electrolysis was experimentally confirmed via XRD in addition to thermodynamic calculations.

4.5. Behaviors of the constituent elements during electrolysis in Exp. 1 and 2

Second, the distribution of elements between the molten salt and the solid phase was analyzed. Fig. 11 plots the distributions in (a) Exp. 1 and (b) Exp. 2, which are obtained from the data listed in Table 5. The distribution data are plotted as a graph with the value of the molten salt on the horizontal axis and the value of the solid phase on the vertical axis after the electrolysis. Note again that the data for molten salt in Exp. 1 were influenced by both the immersion and electrolysis experiments because the molten salt was sampled after the completion of all the experiments in the same melt.

The behavior of the elements will now be discussed by categorizing them into six groups: (1) alkali and alkaline earth elements, (2) Si, B, Al, and Zr, (their oxides are the

main components of the glass and expected to show similar behaviors) (3) REEs, (4) precious metal elements, (5) Se, Te, and Zn, (elements that are expected to be evaporated as gas), and (6) other transition elements.

4.5.1 Group 1: Alkali and alkaline earth elements (Li, Na, Rb, Cs, Sr, Ba, and Ca)

Nearly all the alkali and alkaline earth elements, including Cs, one of the LLFPs, were dissolved into the $CaCl_2$ molten salt in both Exp. 1 and 2. This result is consistent with the thermodynamic prediction discussed in Sections 3.1, 3.2.1, and 3.2.3, and our previous papers [6,7]. The only discrepancy was the small distribution ratio of Li into the molten salt in Exp. 2. Lithium might have been intercalated in the large graphite crucible used as a cathode. The behavior of Ca cannot be quantitatively discussed because the melt was $CaCl_2$. CaO in simulant 3 may be dissolved as Ca^{2+} and O^{2-} ions, slightly decreasing the value of pO^{2-} in the system.

4.5.2 Group 2: Si, B, Al, and Zr

These elements are the main components of simulant 3. Their electrochemical reduction behavior in molten $CaCl_2$ has already been discussed in our previous papers [6,7]. Silicon mainly remained in the solid phase and slightly dissolved into the molten salt in Exp. 1, while it was not detected from the molten salt in Exp. 2. The dissolution of Si in the molten salt might be caused by the dissolution of calcium silicate into $CaCl_2$. The formation of Si and Ru_2Si_3 was confirmed at 1.1 V or more negative potential in Exp. 1 and at 0.6 V in Exp. 2. According to the potential–pO^{2-} diagram for Si (Fig.4a), the stable region of Si is $pO^{2-} > 3.98$ at 1.1 V. Considering that the calculated pO^{2-} value is approximately 2.50 in Exp. 1, the experimental results seem slightly

incompatible with the calculation results. This incompatibility is explained by the fact that the actual pO^{2-} value was higher than the calculated value, because it was calculated by assuming that all the oxides in simulant 3 dissolved as O^{2-} ions and excluded the consumption of O^{2-} ions at the anode. As explained in Section 4.2, the pO^{2-} value will be high especially at the beginning of the electrolysis.

Boron remained in the solid phase but partially dissolved into the molten salt. The dissolution ratio of B in Exp. 2 was larger than that in Exp. 1. Because calcium borates have certain solubility in molten $CaCl_2$, they were partially dissolved in both Exp.1 and 2. On the other hand, B hardly dissolves from XB_6 (X = Ca, Si, or REEs), which was formed in Exp. 1 but not in Exp. 2, as discussed in Sections 4.2 and 4.3. This is why the dissolution ratio in Exp. 2 was higher than that in Exp. 1.

Most of Al and Zr remained in the solid phase. The formation of $Al_{1.77}Ca_{0.88}O_8Si_{2.23}$, which was confirmed via XRD in Exp. 2, corroborates the retention of Al in the solid phase in Exp. 2. Zirconium, one of the LLFPs, stayed in the solid phase in both Exp. 1 and 2. According to the potential–pO^{2-} diagram for the Zr system (Fig. 4g), all the stable phases at approximately pO^{2-} = 2.50 (estimated value for Exp. 1) and at pO^{2-} =1.14 (estimated value for Exp. 2) are solid. Therefore, the retention of Zr in the solid phase is reasonable.

4.5.3 Group 3: Rare earth elements (Y, La, Ce, Pr, Nd, Sm, Eu, and Gd)

As already discussed in Sections 4.2 and 4.3, the formation of REB_6 was confirmed in Exp. 1 but not in Exp. 2. In addition, nearly all the REEs remained in the solid products and partially dissolved into the molten salt (up to 35% in Exp. 1). In Exp. 2, they were not detected in the molten salt except for a small value of Eu. According to the potential–pO^{2-} diagrams, the oxides of Y, Ce, Pr, and Gd, the oxychlorides of La

and Nd, and the ions of Sm and Eu are stable at approximately pO^{2-} = 2.50 (estimated value for Exp.1) and E = 0.6 V. In Exp. 1, the behaviors of these elements are not completely consistent with thermodynamic expectations. Considering reaction (2), the present tendency between Exp.1 and Exp.2 is reasonable, i.e., the partial dissolution of REO_x is suppressed as the pO^{2-} value decreases. In Exp.2, most part of Sm and Eu remained in the solid phase as well as other REEs. The behaviors of REEs except Sm and Eu are consistent with thermodynamic expectations. From the diagram for Sm at pO^{2-} = 1.14 (estimated value for Exp.2), Sm is predicted to be ions (E < 0.73 V). Also, Eu is predicted to be in the form of ions at a more negative potential than 1.8 V at pO^{2-} = 1.14. Contrary to the thermodynamic expectations, most Sm and Eu remained in the solid as abovementioned. The remained Sm and Eu may have been fixed in oxides or oxychlorides of other REEs.

4.5.4 Group 4: Precious metal elements (Pd, Ru, Rh, and Ag)

The precious metals, including Pd, which is one of the LLFPs, were stable in their metallic state, and most of the Pd in simulant 3 was detected in the solid phase. This behavior is in good agreement with the potential–pO^{2-} diagram (Fig. 4i) and reduction behavior of simulant 2 [7].

The behaviors of Ru in Exp. 1 and Exp. 2 have been partly discussed in Sections 4.2 and 4.3, respectively. In Exp. 1, the formation of Ru was indicated in the cases of immersion and electrolysis at 1.4 V. The formation of Ru_2Si_3 was also indicated in the cases of electrolysis at 1.1 V or more negative potentials. In Exp. 2, Ru_2Si_3 was observed from the reduction products. According to the results of ICP-AES and -MS, Ru was mostly detected in the solid part in both Exp.1 and Exp.2, which is reasonably explained by the potential–pO^{2-} diagram (Fig. 5m).

Although Rh was not detected via XRD, most of the Rh was detected from the solid part without dissolution. As with Ru, the behavior is reasonable from the thermodynamic calculation (Fig. 5n).

The detection of Ag in the molten salt in Exp. 1 is attributed to the contamination from the Ag^+/Ag reference electrode. From the results of Exp. 2, most of the Ag in simulant 3 stayed in the solid products similarly to Ru and Rh, which is also reasonable from the thermodynamic calculation (Fig. 5o).

4.5.5 Group 5: Se, Te, and Zn

Although Se and Te are both group 16 elements (chalcogens), their behaviors were quite different in the present study. The evaporation of Se and Zn from the system has already been reported in one of our previous studies [7].

Since some compounds, such as $Se_2(g)$, $SeO_2(g)$, and $ZnCl_2(l)$, are volatile, the distributions in both the solid phase and the molten salt were small for Zn and Se in Exp. 2. According to Fig. 4f, there is a large region of $ZnCl_2(l)$ in the potential–pO^{2-} diagram, expressed as Zn^{2+} having an activity of 10^{-2}. Since $ZnCl_2(l)$ with an activity of 0.01 has a vapor pressure of 2.68×10^{-2} atm at 1103 K, $ZnCl_2$ probably evaporated from the melt and extracted from the experimental system with Ar-gas flow.

$$\mathrm{ZnO}\ (s,\ \textit{in glass}) + \mathrm{CaCl_2}\ (l) \rightarrow \mathrm{ZnCl_2}\ (l,\ \textit{in molten salt}) + \mathrm{CaO}\ (l) \qquad (11)$$

$$\mathrm{ZnCl_2}\ (l,\ \textit{in molten salt}) \rightarrow \mathrm{ZnCl_2}\ (g) \qquad (12)$$

The reason for the remaining Zn in the solid part in Exp. 1 is probably the high reduction rate of ZnO and retention as solid alloys containing Zn. On the other hand, in Exp. 2, the potential was not constant; therefore, most of Zn evaporated as $ZnCl_2(g)$ within the

first 2 h. From the immersion results, the distribution ratio of Zn in the solid was 41%. The rest of the Zn seems to be partially evaporated as $ZnCl_2(g)$.

Selenium, one of the LLPF elements, disappeared from the system in Exp. 2, though it was partially dissolved in the molten salt in Exp. 1. According to Sakamura *et al.*, Se^{2-} ions are stable in LiCl–KCl melt and vaporized as Se_2 gas at the anode (Eq. 13) [69]. Owing to the lack of thermodynamic data for Se^{2-} ions, they were not considered in our thermodynamic calculation (Fig. 4j). However, Se^{2-} ions may be formed by the formation and dissolution of CaSe (Eq. (14) and (15)) or by the direct reduction of SeO_2 (Eq. (16)) during electrolysis. Thus, the loss of Se in Exp. 2 is attributable to the generation and vaporization of Se_2(g) at the anode.

$$2\ Se^{2-} \rightarrow Se_2\ (g) + 4\ e^- \qquad \text{(Anode)} \qquad (13)$$

$$SeO_2(s, \text{in glass}) + 4\ e^- + Ca^{2+} \rightarrow CaSe + 2\ O^{2-} \qquad \text{(Cathode)} \qquad (14)$$

$$CaSe \rightarrow Se^{2-} + Ca^{2+} \qquad (15)$$

$$SeO_2(s, \text{in glass}) + 6\ e^- \rightarrow Se^{2-} + 2\ O^{2-} \qquad \text{(Cathode)} \qquad (16)$$

The reason for the partial remaining of Se in the solid part in Exp. 1 is probably the slow dissolution of CaSe(*s*). The behavior of Se, i.e., evaporation from the system during the electrolysis, is similar to that observed in our previous work using simulant 2 [7].

The ICP-AES and -MS results showed that Te mostly stayed in the solid phase. From the potential–pO^{2-} diagram (Fig. 5r), Te was expected to remain as metallic Te(*l*) or CaTe(*s*). Sakamura *et al.* reported the behavior of Te^{2-} ions in LiCl–KCl melt [69]. Although the melt is different, there is a possibility of Te^{2-} ions to exist in $CaCl_2$.

4.5.6 Group 6: Other transition elements (Sn, Cr, Mn, Fe, Ni, and Mo)

Since the concentrations of these transition elements, especially Cr and Ni, in simulant 3 are too small, and some of them were used in the experimental apparatus in Exp. 1, the distribution ratios for Exp. 1 should be ignored. Therefore, their behaviors are discussed based on the results of Exp. 2.

These elements are in the transition metals group and they have relatively large stable regions of their metallic state or Ca–M alloy ($Ca_2Sn(s)$) in the potential–pO^{2-} diagrams at potentials more negative than 1.0 V. They mostly stayed in the solid part, although Mo was slightly dissolved into the molten salt. According to the potential–pO^{2-} diagram for Mo (Fig.5w), the small dissolution of Mo is possibly caused by the dissolution of $CaMoO_3$ and/or $CaMoO_4(s)$.

Table 6 summarizes the abovementioned behavior of each element in simulant 3 after electrolysis in molten $CaCl_2$. In the future study, additional experiments using gas analysis are needed for Zn and Se to clarify the behavior of these elements.

5. Conclusions

The electrochemical reduction behavior of simulant 3, produced by melting oxides of 33 different elements, including LLFP elements (Cs, Se, Zr, and Pd), was investigated in molten $CaCl_2$ at 1103 K for the treatment of vitrified nuclear waste. First, the potential−pO^{2-} diagrams were constructed to predict the behaviors of the constituent elements. Although U was not present in simulant 3, the diagram for U was also constructed. Second, in Exp. 1, small crucible electrodes containing approximately 100 mg of the simulant were electrolyzed at several potentials for 1 h. The reduction products at 1.1 V or more negative potentials were indicated to contain Si, Ru_2Si_3, and XB_6 (X =Ca, Si, or REE). Third, in Exp. 2, a large crucible electrode containing

approximately 10 g of the simulant was galvanostatically reduced for 5 h. From the analysis of the reduction products and molten salt obtained in Exp. 1 and 2, Si and Zr (LLFP) were indicated to remain in the reduced product. Alkali and alkaline earth elements, including Cs (LLFP), were confirmed to dissolve into molten $CaCl_2$. Precious metal elements, including Pd (LLFP), stayed in the solid phase. These behaviors were common to both Exp. 1 and 2. On the other hand, Zn and Se (LLFP) were indicated to partially evaporate from the system, especially when long-term electrolysis was conducted as in Exp. 2. Most of the elements' behaviors were reasonably explained by the potential−pO^{2-} diagrams.

Acknowledgments

The authors thank Mr. Junichi Imaru (Graduate School of Energy Science, Kyoto University) for his assistance in manufacturing the glass-seal electrodes and Mr. Shohei Kanamura for insightful discussions and his assistance in the ICP-MS measurements.

Funding: This work was funded by the ImPACT Program of the Council for Science, Technology and Innovation (Cabinet Office, Government of Japan). One of the authors (Y. K.) was supported in part by MEXT/JSPS KAKENHI 17J08901.

References

[1] T. Mukaiyama, T. Takizuka, M. Mizumoto, Y. Ikeda, T. Ogawa, A. Hasegawa, H. Takada, H. Takano, Prog. Nucl. Energy. 38 (2001) 107–134 doi:10.1016/S0149-1970(00)00098-6.

[2] Japan Society and Technology Agency, Impulsing Paradigm Change through Disruptive Technologies Program. Reduction and Resource Recycle of High Level Radioactive Wastes with Nuclear Transmutation. http://www.jst.go.jp/impact/en/program/08.html (accessed September 29, 2017).

[3] H. Wang, H. Otsu, H. Sakurai, D. Ahn, M. Aikawa, T. Ando, S. Araki, S. Chen, N. Chiga, P. Doornenbal, N. Fukuda, T. Isobe, S. Kawakami, S. Kawase, T. Kin, Y. Kondo, S. Koyama, S. Kubono, Y. Maeda, A. Makinaga, M. Matsushita, T. Matsuzaki, S. Michimasa, S. Momiyama, S. Nagamine, T. Nakamura, K. Nakano, M. Niikura, T. Ozaki, A. Saito, T. Saito, Y. Shiga, M. Shikata, Y. Shimizu, S. Shimoura, T. Sumikama, P.A. Söderström, H. Suzuki, H. Takeda, S. Takeuchi, R. Taniuchi, Y. Togano, J. Tsubota, M. Uesaka, Y. Watanabe, Y. Watanabe, K. Wimmer, T. Yamamoto, K. Yoshida, Prog. Theor. Exp. Phys. 2017 (2017) 1–10 doi:10.1093/ptep/ptw187.

[4] Z.C. Zhu, W. Luo, Z.C. Li, Y.M. Song, X.D. Wang, X.L. Wang, G.T. Fan, Ann. Nucl. Energy. 89 (2016) 109–114 doi:10.1016/j.anucene.2015.11.017.

[5] Y. Katasho, X. Yang, K. Yasuda, T. Nohira, J. Electrochem. Soc. 163 (2016) D622–D627 doi:10.1149/2.0971610jes.

[6] Y. Katasho, K. Yasuda, T. Nohira, J. Electrochem. Soc. 164 (2017) D478–D485 doi:10.1149/2.1201707jes.

[7] Y. Katasho, K. Yasuda, T. Nohira, J. Nucl. Mater. 503 (2018) 290–303 doi:10.1016/j.jnucmat.2018.03.006.

[8] K. Yasuda, T. Nohira, R. Hagiwara, Y.H. Ogata, J. Electrochem. Soc. 154 (2007) E95–E101 doi:10.1149/1.2736641.

[9] X. Yang, K. Yasuda, T. Nohira, R. Hagiwara, T. Homma, J. Electrochem. Soc. 161 (2014) D3116–D3119 doi:10.1149/2.017407jes.

[10] Landolt-Börnstein, Thermodynamic Properties of Inorganic Material, Scientific Group Thermodata Europe (SGTE), Springer-Verlag, Berlin-Heidelberg, 1999.

[11] Glushko, Thermocenter of the Russian Academy of Sciences, Moscow, Russia, 1994.

[12] I. Barin, Thermochemical Data of Pure Substances, VCH Verlags Gesellschaft, Weinheim, 1989.

[13] I. Barin, Thermochemical Data of Pure Substances, Part I and Part II, VCH Verlags Gesellschaft, Weinheim, 1993.

[14] A.J. Bard, R. Parsons, J. Jordan, Standard potentials in aqueous solution, Marcel Dekker Inc., New York, 1985.

[15] G. Ottonello, M. Attene, D. Ameglio, D. Belmonte, M.V. Zuccolini, M. Natali, Chem. Geol. 346 (2013) 81–92.

[16] G. Eriksson, P. Wu, M. Blander, A.D. Pelton, Can. Metall. Q. 33 (2014) 13–21.

[17] T. Toba, K. Yasuda, T. Nohira, X. Yang, R. Hagiwara, K. Ichitsubo, K. Masuda, T. Homma, Electrochemistry. 81 (2013) 559–565.

[18] A.V. Blinder, S.P. Goridienko, É.V. Marek, V.B. Muratov, Powder Metall. Met. Ceram., 36 (1997) 409–412.

[19] M.W. Chase, C.A. Davies, J.R. Downey, J. Frurip D., R.A. McDonald, A.N. Syverud, J. Phys. Chem. Ref. Data. 14 (1985).

[20] G. Belov., V. Iorish, V. Yungman, IVTANTHERMO - database on thermodynamic properties and related software, Calphad 23, 2 (1999) 173–18

[21] W. Zhuang, J. Liang, Z. Qiao, J. Shen, Y. Shi, G. Rao, J. Alloys Compd. 267 (1998) 6–10.

[22] V.P. Itkin, C.B. Alcock, P.J. van Ekeren, H.A.J. Oonk, J. Phase Equilib. 9 (1988) 652–657.

[23] H. Kadowaki, Y. Katasho, K. Yasuda, T. Nohira, J. Electrochem. Soc. 165 (2018) D83–D89.

[24] TC RAS Thermodynamic Database for Organic Compounds, 2000 Species, 1986.

[25] Glushko, Thermocenter of the Russian Academy of Sciences, Moscow, Russia, 1996.

[26] P. Patnaik, Handbook of Inorganic Chemicals, McGraw-Hill, New York, 2003.

[27] THERMODATA, Grenoble Campus, 1001 Avenue Centrale, BP 66, F-38402 Saint Martin d'Héres, France, 1993.

[28] O. Knacke, O. Kubaschewski, K. Hesselman, Thermochemical Properties of Inorganic Substances, 2nd ed., Springer-Verlag, Berlin, 1991.

[29] N.N. Smirnova, T.A. Bykova, N.A. Polotnyanko, N.D. Shikina, I.L. Khodakovskii, Low-Temperature Heat Capacity and Standard Entropy of PdO (cr.), Russ. J. Phys. Chem. A, 84(11) (2010) 1851–1855.

[30] C.L. Yaws, The YAWS handbook of Thermodynamic properties for Hydrocarbons and Chemicals, Houston, 2006.

[31] Olin Åke, Chemical Thermodynamics of Selenium, Chemical Thermodynamics vol. 7, pp. 40-86, Elsevier B.V., Amsterdam, 2005.

[32] I. Barin, O. Knacke, O. Kubaschewski, Thermochemical Properties of Inorganic Substances, Supplement, Springer-Verlag, Berlin and New York, 1977.

[33] Scientific Group Thermodata Europe, Grenoble Campus, 1001 Avenue Centrale, BP 66, F-38402 Saint Martin d'Héres, France, 1999.

[34] Scientific Group Thermodata Europe, Grenoble Campus, 1001 Avenue Centrale, BP 66, F-38402 Saint Martin d'Héres, France, 1994.

[35] M. Chase, NIST-JANAF, Thermochemical Tables - Fourth Edition, J. of Phys. and Chem. Ref. Data, Mononograph No. 9, 1998.

[36] L.V. Gurvich, I.V. Veitz, Thermodynamic Properties of Individual Substances. Fourth edition in 5 volumes, Vol 1 in 2 parts, Fourth edi, Hemisphere Pub Co. NY, 1989.

[37] E. H. P. Cordfunke, A. S. Booij, R. R. van der Laan, The thermochemical properties of Y2Si2O7 and Dy2Si2O7, Journal of Chemical Thermodynamics, Vol. 30, pp. 199-205, 1998.

[38] M. Binnewies, E. Milke, Thermochemical Data of Elements and Compounds, 2nd edition, Wiley-VCH, Weinheim, 2002.

[39] M.E. Huntelaar, A.S. Booij, E.H.P. Cordfunke, R.R. van der Laan, J.C. van Genderen, A.C.G., van Miltenburg, J. Chem. Thermodyn. 32 (2000) 465–482.

[40] A. D. Chervonnyi, N. A. Chervonnaya, The Standard Thermodynamic Properties of 4f Metal Dichlorides, Russ. J. Phys. Chem. A, 82(2) (2008) 184–192.

[41] L. Rycerz, M. Gaune-Escard, Thermodynamics of SmCl3 and TmCl3: Experimental Enthalpy of Fusion and Heat Capacity. Estimation of Thermodynamic Functions up to 1300 K, Z. Naturforsch. 57 a (2002) 79–84.

[42] L.P. Ruzinov, B.S. Guljanickij, Ravnovesnye prevrasoenija metallugiceskin reaktseij, Moskva, 1975.

[43] J. B. Burns, J. R. Peterson, R. G. Haire, Standard enthalpies of formation for europium, gadolinium, and lutetium oxychlorides, calculated from measured enthalpies of solution, J. Alloys Compd., 265 (1998) 146–152.

[44] Slop, http://zonvark.wustl.edu/geopig/index.html, Everett Shock, Department of Earth and Planetary Sciences, Washington University, One Brookings Drive, St Louis MO, 1998.

[45] R. A. Robie, B. S. Hemingway, Thermodynamic Properties of Minerals and Related Substances at 298.15 K and 1 Bar (105 Pascals) Pressure and at Higher Temperatures, U.S. Geological Survey Bulletin 2131, 1995.

[46] H. Yokokawa, N. Sakai, T. Kawada, M. Dokiya, J. Solid State Chem. 94 (1991) 106–120.

[47] HSC Chemistry 9.8.1.2 (Outotec). https://www.outotec.com/products/digital-solutions/hsc-chemistry/

[48] I. Uchida, J. Niikura, S. Toshima, J. Electroanal. Chem. Interfacial Electrochem. 124 (1981) 165–177 doi:10.1016/S0022-0728(81)80294-X.

[49] L.D. Brown, R. Abdulaziz, R. Jervis, V.J. Bharath, R.C. Attwood, C. Reinhard, L.D. Connor, S.J.R. Simons, D. Inman, D.J.L. Brett, P.R. Shearing, J. Nucl. Mater. 464 (2015) 256–262 doi:10.1016/j.jnucmat.2015.04.037.

[50] R. Abdulaziz, L.D. Brown, I. Douglas, S. Stefaan, P.R. Shearing, D.J.L. Brett, Int. J. Electrochem. Sci. 11 (2016) 10417–10435 doi:10.20964/2016.12.27.

[51] L.D. Brown, R. Abdulaziz, S. Simons, D. Inman, D.J.L. Brett, P.R. Shearing, J. Appl. Electrochem. 43 (2013) 1235–1241. doi:10.1007/s10800-013-0611-9.

[52] Y. Castrillejo, M.R. Bermejo, R. Pardo, A.M. Martínez, J. Electroanal. Chem. 522 (2002) 124–140 doi:10.1016/S0022-0728(02)00717-9.

[53] Y. Sakamura, Electrochim. Acta. 80 (2012) 308–315 doi:10.1016/j.electacta.2012.07.027.

[54] Y. Shen, J. Zhang, J. Rare Earths, 35 (2017) 187–192 doi:10.1016/S1002-0721(17)60898-6.

[55] S. Park, J. Yun, J. Rare Earths, (2019) 1–8, doi:10.1016/j.jre.2019.06.008.

[56] H. Hayashi, K. Minato, J. Phys. Chem. Solids, 66 (2005) 422–426 doi:10.1016/j.jpcs.2004.06.054.

[57] L. Perring, F. Bussy, J. C. Gachon, and P. Feschotte, J. Alloys Compd., 284 (1999) 198–205 doi:10.1016/S0925-8388(98)00911-6

[58] H. Yin, D. Tang, X. Mao, W. Xiao, D. Wang, J. Mater. Chem. A. 3 (2015) 15184–15189 doi:10.1039/C5TA03728J.

[59] E.F. Westrum, J.T.S.J. Andrews, B.H. Justice, D.A. Johnson, J. Chem. Thermodyn. 34 (2002) 239–250.

[60] S. Kosolapovoi T.G., Polysenie i primenie tugoplavkih soedinenij., Moskva, 1986.

[61] Borovikova, M.S., Fesenko, V.V. *J. of the Less-Common Metals*, 117, (1986), 287–291.

[62] M. Kamaludeen, I. Selvaraj, A. Visuvasam, R. Jayavel, J. Mater. Chem. 8 (1998) 2205–2207 doi:10.1039/a802895h.

[63] K. Amalajyothi, L.J. Berchmans, S. Angappan, A. Visuvasam, 310 (2008) 3376–3379 doi:10.1016/j.jcrysgro.2008.04.026.

[64] G.A. Bukatova, S.A. Kuznetsov, M. Gaune-Escard, Russ. J. Electrochem. 43 (2007) 929–935 doi:10.1134/S1023193507080113.

[65] G.A. Bukatova, S.A. Kuznetsov, Electrochem. Commun. 7 (2005) 637–641 doi:10.1016/j.elecom.2005.04.003.

[66] J. Yang, S. Lu, S. Kan, X. Zhang, J. Du, Chem. Commun. (Cambridge, U. K.). (2009) 3273–3275 doi:10.1039/b902029b.

[67] J. Zhao, J. Li, P. Ying, W. Zhang, L. Meng, C. Li, Chem. Commun. (Cambridge, U. K.). 49 (2013) 4477–4479 doi:10.1039/c3cc00101f.

[68] Y. Nishimura, T. Nohira, K. Kobayashi, R. Hagiwara, J. Electrochem. Soc. 158 (2011) E55–E59 doi:10.1149/1.3575635.

[69] Y. Sakamura, T. Murakami and K. Uozumi, J. Electrochem. Soc. 167 (2020) 082511 doi:10.1149/1945-7111/ab904e.

Tables

Table 1. Composition of four types of glasses used in our previous studies and the present study: Pyrex® glass, simulant 1 (glass component only), simulant 2 (containing LLFPs: Zr, Cs, Pd, and Se), and simulant 3 (nearly the same composition as real vitrified waste).

	Pyrex® glass	Simulant 1	Simulant 2		Simulant 3	
Electrochemical reduction in molten salt	Ref [5,6]	Ref [7]	Ref [7]		This study	
Softening point	1093 K	863 K	873 K		unknown	
Composition as oxide / wt%						
SiO_2	80.8	55.4	53.7		48.8	
B_2O_3	12.6	16.8	16.3		14.8	
Na_2O	4.0	11.4	11.1		10.0	
K_2O	0.4	-	-		-	
Al_2O_3	2.3	5.9	5.7		5.2	
CaO	-	3.5	3.4		3.1	
Li_2O	-	3.5	3.4		3.1	
ZnO	-	3.5	3.4		3.1	
LLFP oxide	-	-	ZrO_2	1.5	ZrO_2	1.34
			Cs_2O	1.0	Cs_2O	1.68
			PdO	0.5	PdO	0.40
			SeO_2	0.1	SeO_2	0.02
Other FP oxide	-	-				9.34
Others	-	-		-		0.3

Table 2. Target and analyzed compositions of simulant 3 used in this study.

		Composition	
		Target (wt%)	Analyzed (wt%)
Base glass	SiO_2	48.75	50.5
	B_2O_3	14.79	13.6
	Na_2O	10.00	9.24
	Al_2O_3	5.20	5.47
	CaO	3.09	3.08
	Li_2O	3.09	3.06
	ZnO	3.09	3.21
LLFP oxides	ZrO_2	1.34	1.31
	Cs_2O	0.68	0.71
	PdO	0.40	0.37
	SeO_2	0.02	0.02
Other FP oxides	CeO_2	1.95	1.94
	MoO_3	1.34	1.36
	Gd_2O_3	1.26	1.24
	Nd_2O_3	1.27	1.09
	RuO_2	0.76	0.70
	BaO	0.53	0.54
	Pr_6O_{11}	0.36	0.35
	MnO	0.32	0.34
	La_2O_3	0.39	0.33
	SrO	0.26	0.27
	Sm_2O_3	0.24	0.21
	Fe_2O_3	0.16	0.21
	Y_2O_3	0.16	0.17
	TeO_2	0.16	0.13
	Rh_2O_3	0.14	0.12
	Rb_2O	0.11	0.11
	SnO_2	0.03	0.03
	Eu_2O_3	0.04	0.03
Others	P_2O_5	0.02	0.03
	Ag_2O	0.02	0.02
	NiO	0.02	0.02
	Cr_2O_3	0.01	0.01

Table 3. Thermodynamic data used for the calculations.

System	Compound	Ions shown in E− pO^{2-} diagram	Phase	Standard Gibbs energy of formation / kJ mol^{-1}	References
Ca–O–Cl (Frame)	$CaCl_2$*		Liquid	−629.56	[10]
	CaO*		Solid	−517.42	[10]
	CaO		Liquid	−496.40	[8] This value is limited to molten $CaCl_2$ system.
Si–Ca–O–Cl	$SiCl_4$*		Gas	−515.63	[10,11]
	SiO_2*		Solid	−708.82	[12]
	$CaSiO_3$		Solid	−1316.19	[12]
	$Ca_3Si_2O_7$		Solid	−3217.85	[13,14]
	Ca_3SiO_5		Solid	−2432.17	[15,16]
	$CaSi_2$		Solid	−97.09	[17]
	Ca_3Si_4		Solid	−277.17	[17]
	CaSi		Solid	−88.63	[17]
	Ca_5Si_3		Solid	−358.41	[17]
	Ca_2Si		Solid	−181.38	[17]
B–Ca–O–Cl	BCl_3*		Gas	−346.18	[10]
	B_2O_3*		Liquid	−994.06	[10,13]
	CaB_4O_7		Solid	−2619.79	[10,13,14]
	$Ca_2B_2O_5$		Solid	−2224.55	[13]
	$Ca_3B_2O_6$		Solid	−2798.66	[13]
	CaB_6		Solid	−89.03	[18]
Al–Ca–O–Cl	$AlCl_3$*		Gas	−534.32	[10,19]
	Al_2O_3*		Solid	−1320.71	[20]
	$CaAl_{12}O_{19}$		Solid	−8512.27	[15,16]
	$CaAl_4O_7$		Solid	−3212.13	[15,16]
	$CaAl_2O_4$		Solid	−1867.97	[15]
	$Ca_{12}Al_{14}O_{33}$		Solid	−15790.54	[12]
	$Ca_3Al_2O_6$		Solid	−2927.57	[13,14,21]
	Al–Ca (x_{Ca} = 0.16)		Liquid	−69.05	calculated from [22]
	Al–Ca (x_{Ca} = 0.50)		Liquid	−12.83	calculated from [23]
Li–Ca–O–Cl	LiCl*	Li^+	Liquid	−322.72	[11,13,19,20]
	Li_2O*		Solid	−448.14	[10,11,13]
	$LiClO_4$		Liquid	51.80	[12]
Na–Ca–O–Cl	NaCl*	Na^+	Liquid	−309.25	[10,13,20,24]
	Na_2O*		Solid	−261.37	[12]
	NaO_2		Liquid	−117.91	[20]
Zn–Ca–O–Cl	$ZnCl_2$		Gas	−272.16	[13, 25, 26]
	$ZnCl_2$*	Zn^{2+}	Liquid	−260.75	[10,25]
	ZnO*		Solid	−232.15	[10,25]
Zr–Ca–O–Cl	$ZrCl_4$*		Gas	−739.54	[10,25]
	ZrO_2*		Solid	−886.91	[10,25]
	$CaZrO_3$		Solid	−1439.49	[10,12,27]

Cs–Ca–O–Cl	CsCl*	Cs^+	Liquid	−327.79	[10,11]
	Cs_2O*		Liquid	−181.63	[10,11]
	CsO_2		Liquid	−128.99	[20]
Pd–Ca–O–Cl	$PdCl_2$*	Pd^{2+}	Liquid	−11.91	[28]
	PdO*		Solid	−2.14	[28,29]
Se–Ca–O–Cl	$SeCl_2$		Gas	−47.79	[30]
	SeO_2		Gas	−106.42	[10,11]
	Se		Gas	95.00	[10]
	Se_2		Gas	0.00	[10]
	$SeOCl_2$		Gas	−59.10	[31]
	$CaSeO_4$		Solid	−664.38	[13]
	CaSe		Solid	−331.64	[32]
U–Ca–O–Cl	UCl_3	U^{3+}	Liquid	−628.40	[28]
	UCl_4	U^{4+}	Liquid	−713.98	[10,13]
	UO_2		Solid	−891.26	[10,33]
	U_4O_9		Solid	−3662.48	[10,34]
	U_3O_8		Solid	−2830.01	[10,34]
	UO_2Cl_2	UO_2^{2+}	Liquid	−902.39	[10,28]
	$CaUO_4$		Solid	−1584.37	[32]
Rb–Ca–O–Cl	RbCl*	Rb^+	Liquid	−320.89	[10,11]
	Rb_2O*		Liquid	−176.82	[10,11]
	RbO_2		Liquid	−115.93	[10,11]
Sr–Ca–O–Cl	$SrCl_2$*	Sr^{2+}	Solid	−665.28	[35]
	SrO*		Solid	−482.86	[10,11]
Ba–Ca–O–Cl	$BaCl_2$*	Ba^{2+}	Solid	−680.30	[13,14]
	BaO_2		Solid	−446.56	[10,32]
	BaO*		Solid	−448.19	[10,13]
Y–Ca–O–Cl	YCl_3*	Y^{3+}	Liquid	−743.75	[13]
	Y_2O_3*		Solid	−1579.06	[36]
La–Ca–O–Cl	$LaCl_3$*	La^{3+}	Solid	−802.62	[10,13]
	La_2O_3*		Solid	−1472.25	[13,20,37]
	LaOCl		Solid	−815.70	[12,28,38]
Ce–Ca–O–Cl	$CeCl_3$*	Ce^{3+}	Liquid	−789.68	[10,13,27]
	Ce_2O_3*		Solid	−1486.66	[10,13,39]
	$CeO_{1.72}$		Solid	−798.92	[32]
	$CeO_{1.83}$		Solid	−823.01	[32]
	CeO_2		Solid	−854.35	[10,11,12]
Pr–Ca–O–Cl	$PrCl_3$*	Pr^{3+}	Liquid	−792.78	[13]
	Pr_2O_3*		Solid	−1489.68	[10,11,13]
	$Pr_{12}O_{22}$		Solid	−10518.69	[28]
Nd–Ca–O–Cl	$NdCl_3$*	Nd^{3+}	Liquid	−778.07	[28]
	Nd_2O_3*		Solid	−1490.59	[11,28,37]
	NdOCl		Solid	−793.81	[13]
Sm–Ca–O–Cl	$SmCl_2$	Sm^{2+}	Solid	−622.70	[12,40]**(1000)
	$SmCl_3$*	Sm^{3+}	Liquid	−762.44	[10,34,41]
	Sm_2O_3*		Solid	−1496.05	[10,13,24]
	SmOCl		Solid	−800.81	[28]
Eu–Ca–O–Cl	$EuCl_2$	Eu^{2+}	Liquid	−630.84	[42]

	$EuCl_3$*	Eu^{3+}	Liquid	−663.14	[10,34]
	Eu_2O_3*		Solid	−1317.11	[28,37]
	EuOCl		Solid	−687.47	[42]
Gd–Ca–O–Cl	$GdCl_3$*	Gd^{3+}	Liquid	−762.10	[10,34]**(1000)
	Gd_2O_3*		Solid	−1503.67	[10,11]
	GdOCl		Solid	−778.12	[11,13,43]**(1000)
Ru–Ca–O–Cl	$RuCl_4$*		Gas	52.24	[12]
	RuO_2*		Solid	−118.74	[12]
	RuO_4		Gas	−19.61	[13]
Rh–Ca–O–Cl	$RhCl_3$*	Rh^{3+}	Solid	−19.31	[12,28,38]
	Rh_2O		Solid	−42.92	[32]**(1000)
	Rh_2O_3*		Solid	−55.29	[26,32,44]
Ag–Ca–O–Cl	AgCl*	Ag^{+}	Liquid	−78.24	[10,28,38]
	Ag_2O*		Liquid	38.20	[10]
P–Ca–O–Cl	PCl		Gas	−137.22	[10,35,38]
	PCl_3*		Gas	−361.43	[10,11,13]
	P_2O_3*		Gas	−954.81	[36]
	$POCl_3$		Gas	−569.38	[10,19]
	Ca_3P_2		Solid	−774.44	[13]
	$Ca_2P_2O_7$		Solid	−2930.50	[14,28]
	$Ca_3(PO_4)_2$		Solid	−3592.77	[13]
Sn–Ca–O–Cl	$SnCl_2$	Sn^{2+}	Liquid	−195.19	[10,11]
	$SnCl_4$*		Gas	−316.84	[10,11,28]
	SnO_2*		Solid	−341.42	[13,26,38]
	$SnCl_2O_2$		Gas	−398.79	[10,27]
	$SnCl_2O_4$		Gas	−353.69	[10,27]
	Ca_2Sn		Solid	−258.32	[32]
Te–Ca–O–Cl	$TeCl_2$*		Gas	−134.48	[12,28,38]
	TeO*		Liquid	−122.12	[42]
	TeO_2		Liquid	−115.99	[10,11]
	TeO_3		Gas	57.62	[30]
	$TeCl_2O$		Gas	−127.85	[10,27]
	CaTe		Solid	−257.79	[13]
Cr–Ca–O–Cl	$CrCl_2$	Cr^{2+}	Liquid	−253.85	[10,11]
	$CrCl_3$*	Cr^{3+}	Liquid	−294.94	[10,11]
	$CrCl_4$		Gas	−324.81	[10,11]
	Cr_2O_3*		Solid	−845.24	[35]
	Cr_5O_{12}		Solid	−1875.64	[10,34]
	CrO_2Cl_2		Gas	−401.75	[10,11]
	$CaCr_2O_4$		Solid	−1424.09	[13]
Mn–Ca–O–Cl	$MnCl_2$*	Mn^{2+}	Liquid	−343.88	[20,28]
	MnO*		Solid	−302.43	[10,13,20]
	Mn_3O_4		Solid	−1007.79	[13,20] **(900)
	Mn_2O_3		Solid	−670.03	[20]**(1000)
	MnO_2		Solid	−315.82	[12,26,28,45]
	Mn_2O_7		Liquid	−252.21	[24,34]
Fe–Ca–O–Cl	$FeCl_2$	Fe^{2+}	Liquid	−210.78	[10,25]
	$FeCl_3$*	Fe^{3+}	Liquid	−210.55	[10,25]
	$Fe_{0.947}O$		Solid	−191.69	[34,35,38]

	Fe_3O_4		Solid	−753.04	[12,26]
	Fe_2O_3*		Solid	−530.55	[10,25]
	$CaFe_2O_4$		Solid	−1123.93	[28,45]
	$Ca_2Fe_2O_5$		Solid	−1636.07	[28,45]
Ni–Ca–O–Cl	$NiCl_2$*	Ni^{2+}	Liquid	−138.66	[10,13,25]
	NiO*		Solid	−137.90	[10,33]
Mo–Ca–O–Cl	$MoCl_3$	Mo^{3+}	Liquid	−213.35	[10,27,28]
	$MoCl_4$*	Mo^{4+}	Liquid	−238.02	[35]
	MoO_2*		Solid	−385.03	[10,35,38]
	$MoCl_2O_2$		Gas	−506.52	[35]
	$MoCl_3O$		Gas	−398.64	[10,11]
	$CaMoO_3$		Solid	−949.68	[46]
	$CaMoO_4$		Solid	−1152.93	[12,28,38]

* Species used for the plot in Fig. 3
** Extrapolated data are used for the calculation. The number in parentheses is the highest temperature in K where the data are available.

Table 4. Standard Gibbs energy of formation and redox potential of RE^{3+}, B/REB_6 (RE = Ce, Gd, Nd, La, and Sm).

RE	Ce	Gd*	Nd	La	Sm
ΔG°_f (REB_6) / $kJmol^{-1}$	−311.83 [10, 13]	−126.83 [59]	−160.00 [60]	81.22 [10, 60]	−197.26 [60, 61]
E° (REB_6) vs. RE^{3+}/RE / V	1.08	0.44	0.55	0.28	0.68
E° (RE^{3+}/RE) vs. Ca^{2+}/Ca / V	0.39	0.48	0.43	0.34	−0.19
E° (REB_6) vs. Ca^{2+}/Ca / V	1.46	0.92	0.98	0.62	0.49

* Extrapolated value using data up to 350 K.

Table 5. Results of ICP-AES and -MS analyses for the solid phase and molten salt obtained in Exp. 1 and Exp. 2.

	Distribution of each element/%				
	Exp. 1 (Small crucible)			Exp. 2 (Large crucible)	
	Solid phase	Solid phase*1	Molten salt*1	Solid phase*2	Molten salt*2
	Immersion, 1h	0.6 V, 1 h	After Exp.	−2 A, 5 h	After Exp.
Si	123 [a]	88.8 [a]	9.7	145 [b]	-
Na	1.3 [a]	2.0 [a]	87.7	1.1 [c]	69.9
B	54.9 [a]	86.2 [a]	16.0	68.1 [c]	37.2
Al	116 [a]	90.6 [a]	9.2	92.8 [a]	-
Zn	41.2 [a]	79.7 [a]	1.4	0.7 [c]	-
Ce	67.7 [a]	77.2 [a]	21.8	111 [c]	0.0
Li	3.3 [a]	5.9 [a]	77.1	1.5 [c]	20.1
Gd	87.9 [a]	87.2 [a]	13.0	85.6 [c]	0.0
Zr	112 [a]	99.5 [a]	0.6	71.2 [c]	-
Nd	82.6 [a]	89.5 [a]	19.3	104 [c]	0.0
Mo	11.1 [a]	63.5 [a]	25.0	85.4 [c]	6.1
Cs	13.2 [a]	1.6 [a]	57.7	0.6 [c]	117
Ru	0.4 [b]	72.5 [b]	0.1	86.9 [b]	-
Ba	6.6 [a]	12.5 [a]	87.3	2.6 [a]	118
Pd	76.5 [a]	132 [a]	4.7	101 [b]	-
Pr	78.7 [a]	87.5 [a]	20.6	105 [c]	0.0
La	75.1 [a]	85.7 [a]	28.8	118 [c]	0.0
Mn	32.7 [a]	71.7 [a]	60.8	79.4 [a]	-
Sr	6.0 [a]	13.6 [a]	-	1.7 [a]	132
Sm	89.2 [a]	91.3 [a]	21.4	77.1 [c]	0.0
Fe	110 [a]	111 [a]	56.6	107 [c]	-
Y	87.3 [a]	87.5 [a]	30.2	61.8 [c]	0.0
Te	54.5 [a]	90.2 [a]	13.5	93.3 [b]	-
Rb	4.7 [a]	1.4 [a]	73.9	0.6 [c]	118
Rh	19.0 [b]	93.6 [b]	2.2	85.9 [c]	-
Eu	100 [a]	83.5 [a]	35.0	99.1 [c]	0.2
Sn	96.2 [a]	99.9 [a]	0.8	65.8 [b]	-
Ag	-	59.3 [a]	152	144 [a]	-
Ni	65.7 [a]	496 [a]	13600	92.2 [c]	-
Se	28.7 [a]	54.1 [a]	27.3	13.3 [c]	4.8
Cr	128 [a]	199 [a]	64.9	252 [c]	-

- : Not detected or decreased by electrolysis

a: Subsequent dissolution by 3 mol/L HCl solution and mixture of concentrated HF+HNO_3.

b: Microwave decomposition in mixture of concentrated HNO_3+HCl+HF.

c: Microwave decomposition in mixture of concentrated HNO_3+HCl. For the residue, microwave decomposition in HNO_3+HCl+HF.

*1: The data in these columns are plotted in Fig. 11a.

*2: The data in these columns are plotted in Fig. 11b.

Table 6. Summary of all elements' behaviors for simulant 3.

Element	Exp. 1 Simulant 3: $CaCl_2$ = 1: 500, Minimum pO^{2-} = 2.50	Exp. 2 Simulant 3: $CaCl_2$ = 1: 20 Minimum pO^{2-} = 1.14
Si	Mainly remained in the solid as Si. Partially dissolved	Remained in the solid as Si
B	Mainly remained in the solid (XB_6), partially dissolved	Remained in the solid Partially dissolved
Zr, Al	Remained in the solid	
Cs, Na, Li, Rb, Ba, Sr	Dissolved	
REE (Y, La, Ce, Pr, Nd, Sm, Eu, Gd)	Remained in the solid as REB_6 Slightly dissolved	Remained in the solid
Pd, Ru, Rh, Ag	Remained in the solid in metallic form Formation of $Ru_2Si_3(s)$	
Se	Remained in the solid Partially dissolved	Evaporated ($Se_2(g)$)
Te	Remained in the solid Partially dissolved	Remained in the solid
Zn	Remained in the solid	Evaporated ($ZnCl_2(g)$)
Sn, Cr, Mn, Fe, Ni, Mo	Not evaluated in this study	Remained in the solid
P	Not evaluated in this study	

- : Bold underlined elements are LLFP.

Figure captions

Fig. 1. (a) Schematic of the experimental apparatus in Exp. 1. (A) Working electrode (small crucible), (B) working electrode (simulant glass-sealed electrode), (C) Ag^{+}/Ag reference electrode, (D) graphite counter electrode, and (E) thermocouple. (b) Schematic of the cross section of the small crucible.

Fig. 2. Schematic of the experimental apparatus for electrochemical reduction of a large amount of simulant 3 (Exp. 2).

Fig. 3. Plot of the standard Gibbs energy of formation of oxides and chlorides for the elements present in simulant 3 at 1123 K. The species indicated with asterisks in Table 3 were used for the plot.

Fig. 4. Potential–$p{O}^{2-}$ diagrams for M in molten $CaCl_2$ at 1123 K. M = (a) Si, (b) B, (c) Al, (d) Li, (e) Na, (f) Zn, (g) Zr, (h) Cs, (i) Pd, and (j) Se.

Fig. 5. Potential–$p{O}^{2-}$ diagrams for M in molten $CaCl_2$ at 1123 K. M = (a) U, (b) Rb, (c) Sr, (d) Ba, (e) Y, (f) La, (g) Ce, (h) Pr, (i) Nd, (j) Sm, (k) Eu, (l) Gd, (m) Ru, (n) Rh, (o) Ag, (p) P, (q) Sn, (r) Te, (s) Cr, (t) Mn, (u) Fe, (v) Ni, and (w) Mo.

Fig. 6. (a) Schematic of the vertical half of simulant 3 glass-sealed electrode. Side and bottom views of the glass-sealed electrode (b) before and (c) after cyclic voltammetry. (d) Cyclic voltammograms for the glass-sealed electrode from the 1st cycle to the 5th cycle in molten $CaCl_2$ at 1103 K. Scan rate: 100 mV s^{-1}.

Fig. 7. (a) Cross-sectional micrographs of the samples obtained by immersion or potentiostatic electrolysis of simulant 3. (b) Current transient curves during potentiostatic electrolysis at several potentials for 1 h in molten $CaCl_2$ at 1103

K. (c) Cross-sectional micrographs of the samples obtained by potentiostatic electrolysis of simulant 3 at 0.6 V for several durations.

Fig. 8. (a) XRD patterns of the samples obtained by immersion or potentiostatic electrolysis of simulant 3 at several potentials for 1 h in molten $CaCl_2$ at 1103 K, followed by washing with 3 mol/L HCl solution. (b) Reference XRD patterns of XB_6 (X = Ca, Si, Ce, La, Gd, Nd, and Pr).

Fig. 9. FE-SEM image of the sample obtained by potentiostatic electrolysis of simulant 3 at 0.6 V for 1 h at 1103 K and washing by 3 mol/L HCl solution.

Fig. 10. (a) Potential transient curve during electrolysis in Exp. 2. (b) Photograph of the reduction products obtained by galvanostatic electrolysis of simulant 3 at −2 A for 5 h. Separated products of (A) black power and (B) the remainder with white cylindrical lumps. (c) XRD pattern for the reduction product (A).

Fig. 11. Distribution of elements in molten salt and solid phase in (a) Exp. 1 and (b) Exp. 2.

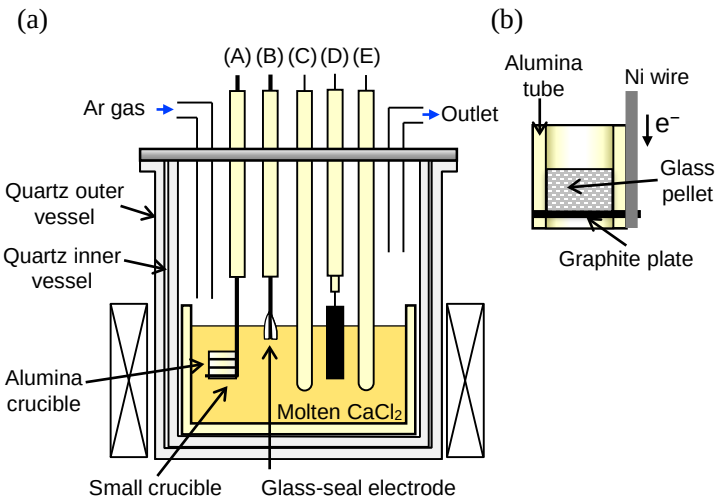

Fig. 1 (a) Schematic of the experimental apparatus in Exp. 1. (A) Working electrode (small crucible), (B) working electrode (simulant glass-sealed electrode), (C) Ag^+/Ag reference electrode, (D) graphite counter electrode, and (E) thermocouple. (b) Schematic of the cross section of the small crucible.

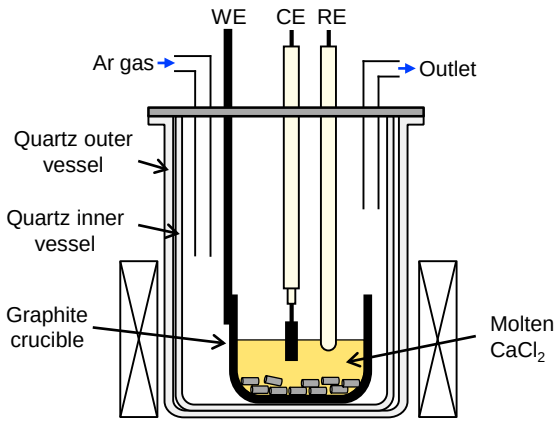

Fig. 2 Schematic of the experimental apparatus for electrochemical reduction of a large amount of simulant 3 (Exp. 2).

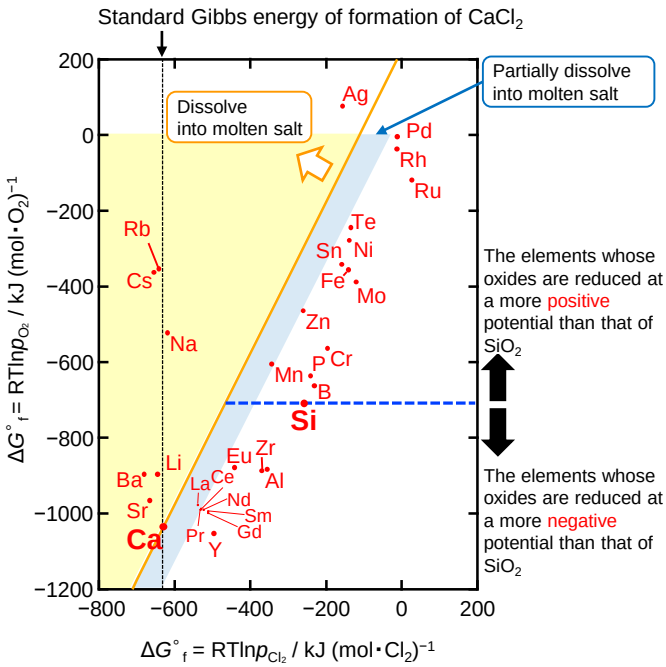

Fig. 3 Plot of the standard Gibbs energy of formation of oxides and chlorides for the elements present in simulant 3 at 1123 K. The species indicated with asterisks in Table 3 were used for the plot.

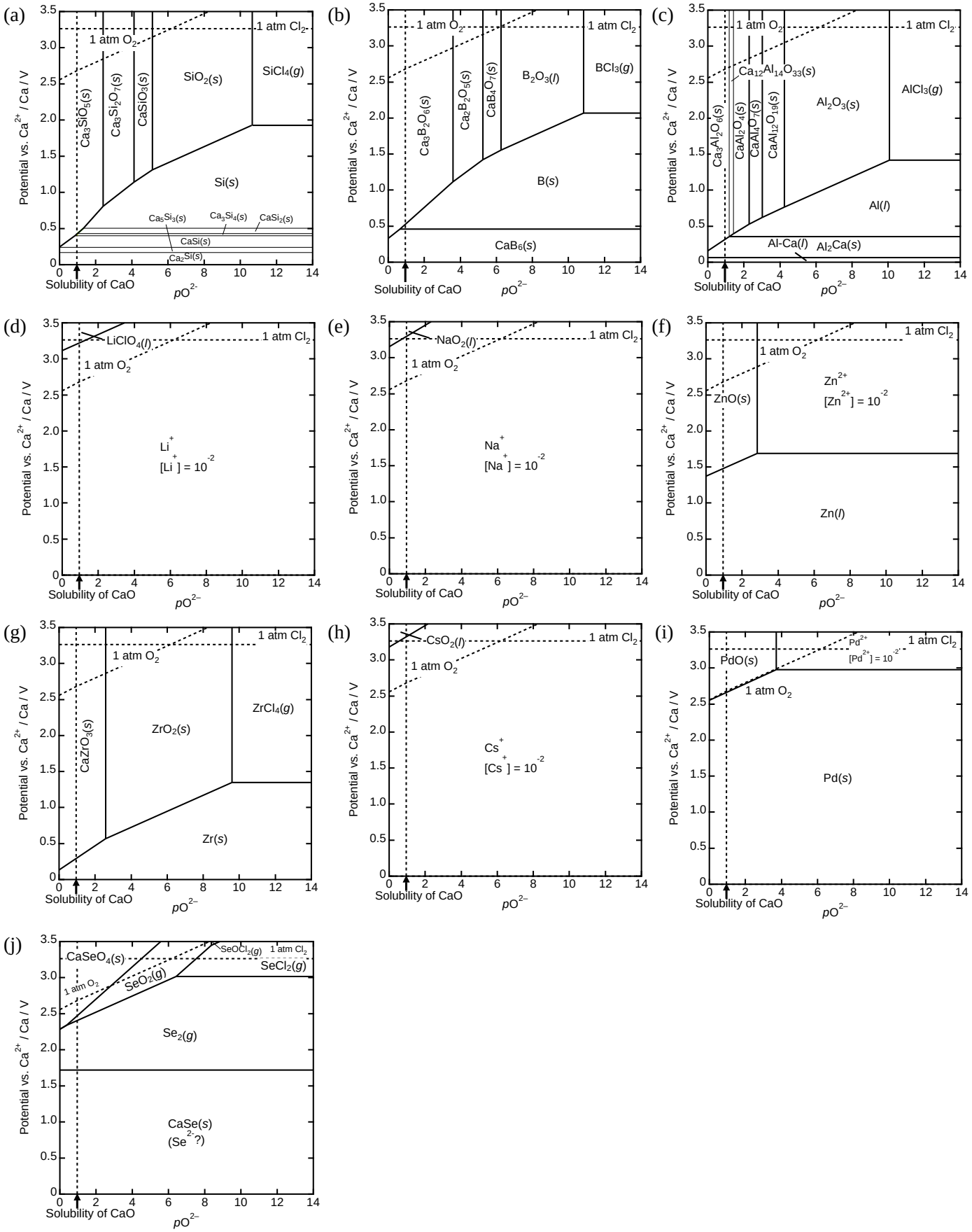

Fig. 4 Potential–pO^{2-} diagrams for M in molten $CaCl_2$ at 1123 K. M = (a) Si, (b) B, (c) Al, (d) Li, (e) Na, (f) Zn, (g) Zr, (h) Cs, (i) Pd, and (j) Se.

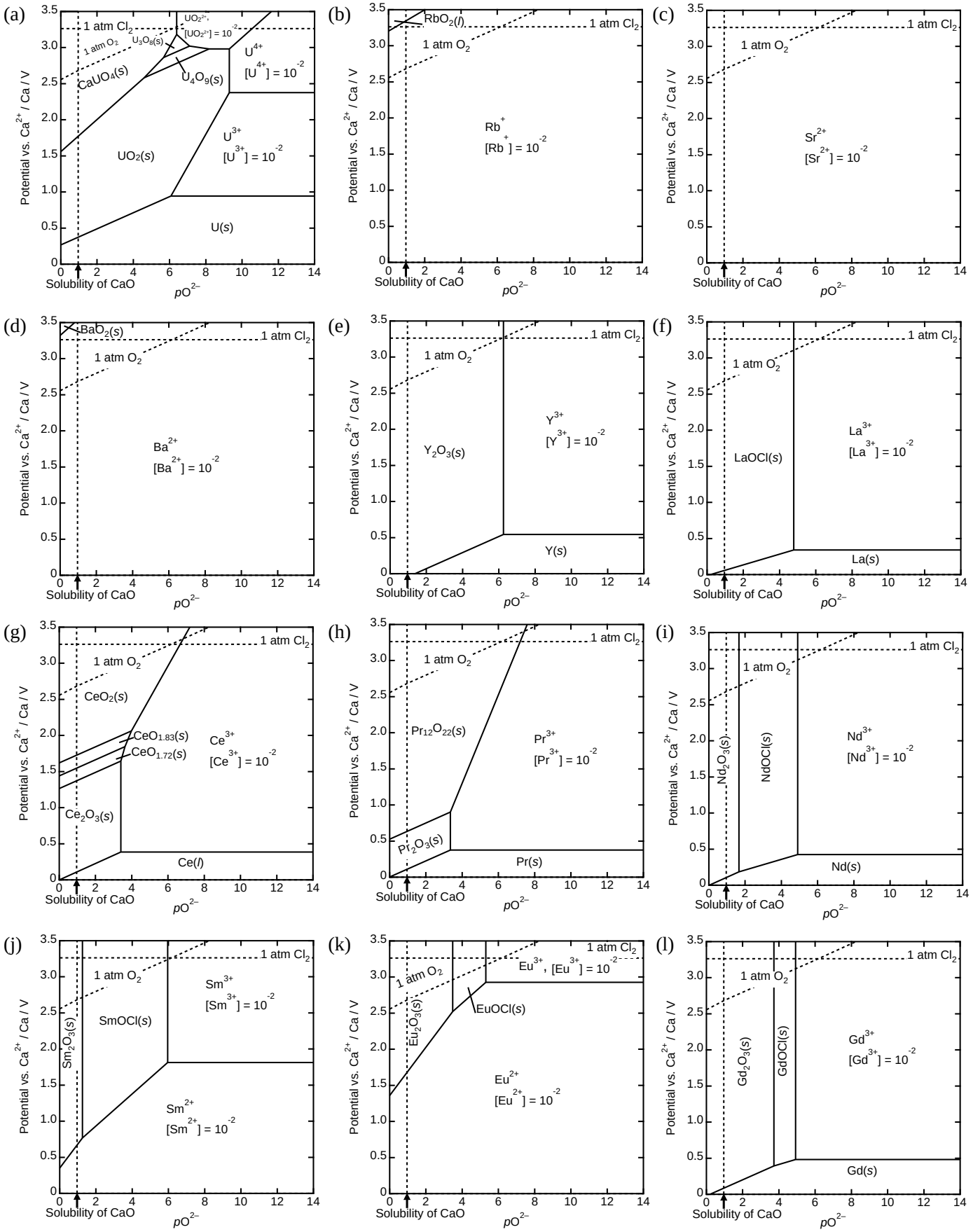

Fig. 5 Potential–pO^{2-} diagrams for M in molten $CaCl_2$ at 1123 K. M = (a) U, (b) Rb, (c) Sr, (d) Ba, (e) Y, (f) La, (g) Ce, (h) Pr, (i) Nd, (j) Sm, (k) Eu, (l) Gd, (to be continued)

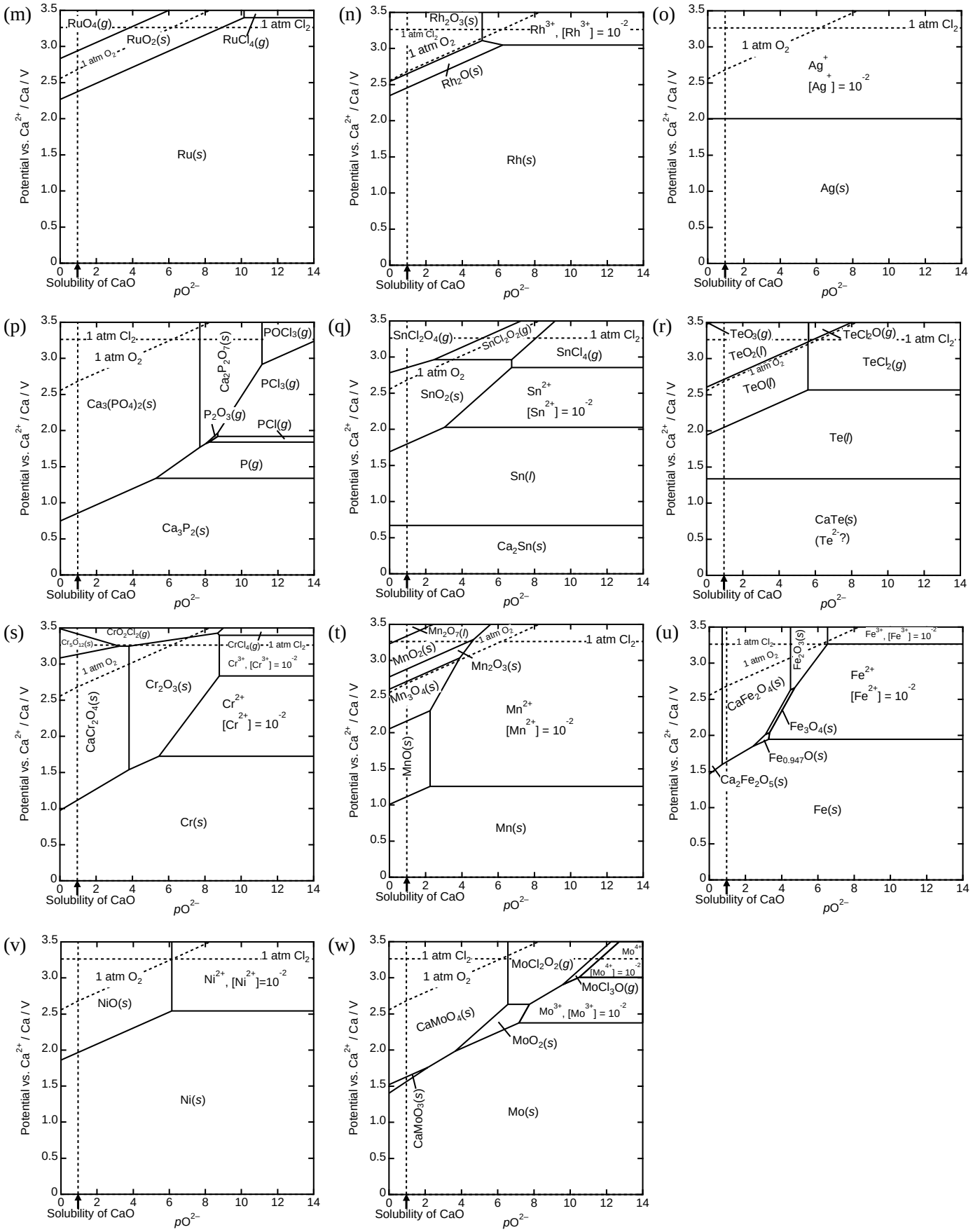

Fig. 5 (Continued) Potential–pO^{2-} diagrams for M in molten $CaCl_2$ at 1123 K. M = (m) Ru, (n) Rh, (o) Ag, (p) P, (q) Sn, (r) Te, (s) Cr, (t) Mn, (u) Fe, (v) Ni, and (w) Mo.

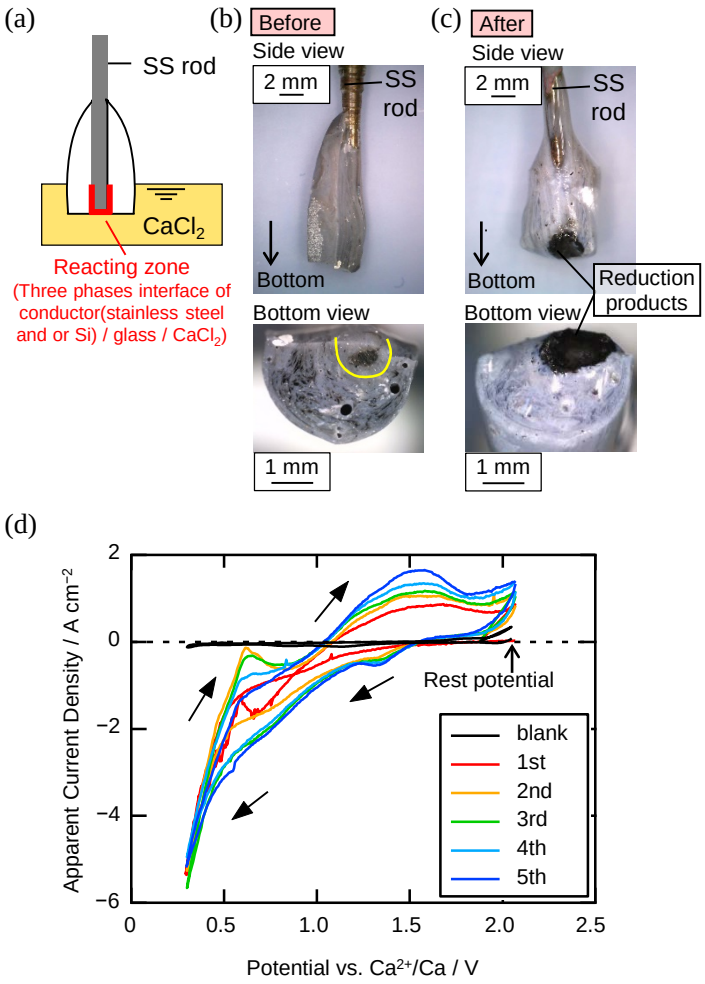

Fig. 6. (a) Schematic of the vertical half of simulant 3 glass-sealed electrode. Side and bottom views of the glass-sealed electrode (b) before and (c) after cyclic voltammetry. (d) Cyclic voltammograms for the glass-sealed electrode from the 1st cycle to the 5th cycle in molten $CaCl_2$ at 1103 K. Scan rate: 100 mV s^{-1}.

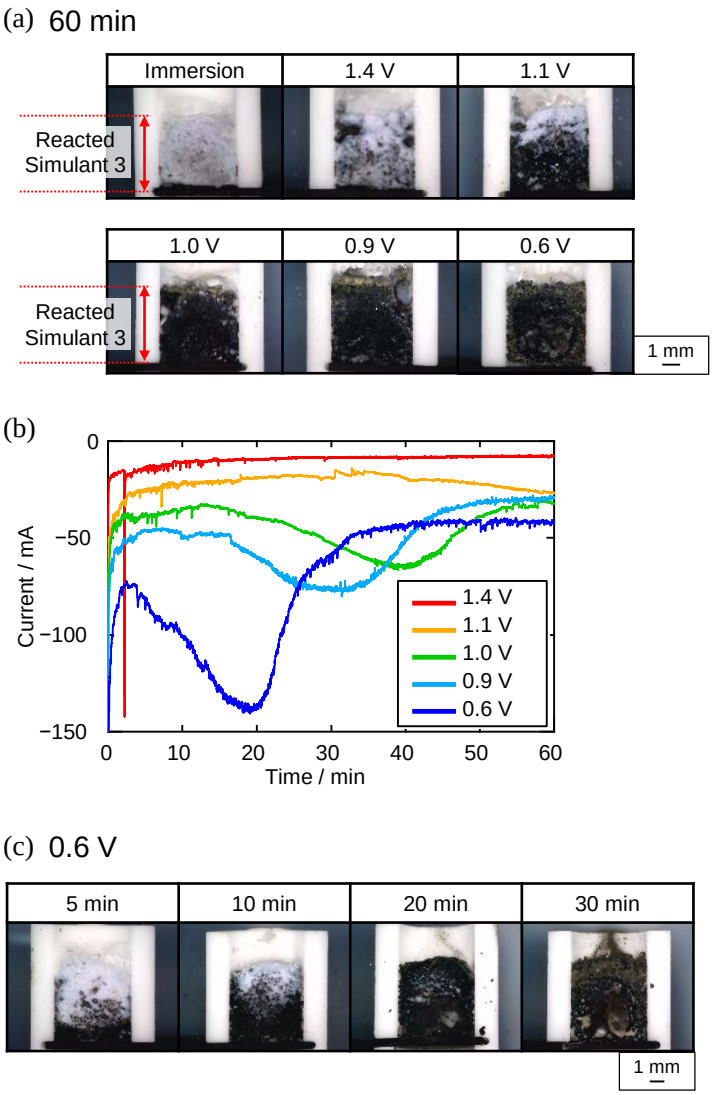

Fig. 7 (a) Cross-sectional micrographs of the samples obtained by immersion or potentiostatic electrolysis of simulant 3. (b) Current transient curves during potentiostatic electrolysis at several potentials for 1 h in molten $CaCl_2$ at 1103 K. (c) Cross-sectional micrographs of the samples obtained by potentiostatic electrolysis of simulant 3 at 0.6 V for several durations.

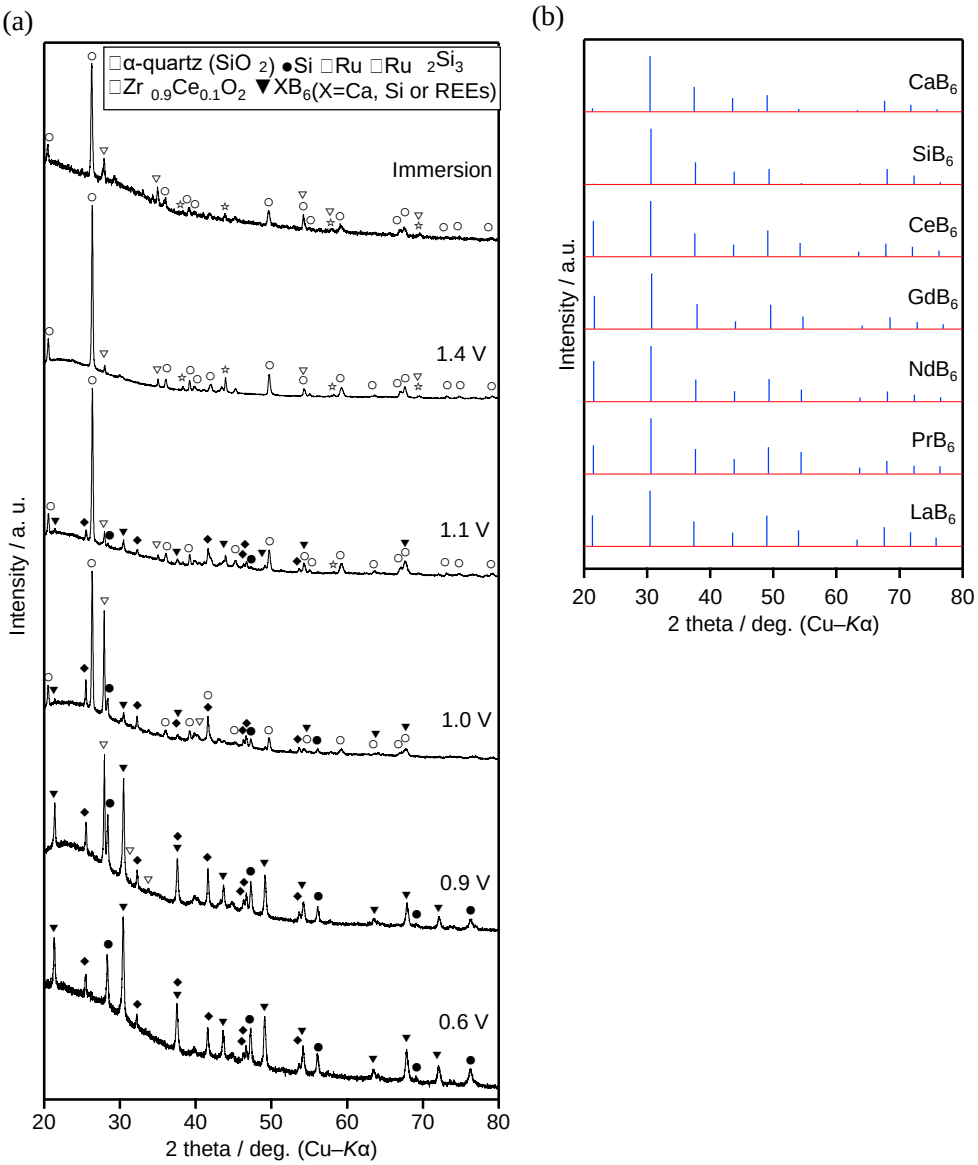

Fig. 8 (a) XRD patterns of the samples obtained by immersion or potentiostatic electrolysis of simulant 3 at several potentials for 1 h in molten $CaCl_2$ at 1103 K, followed by washing with 3 mol/L HCl solution. (b) Reference XRD patterns of XB_6 (X = Ca, Si, Ce, La, Gd, Nd, and Pr).

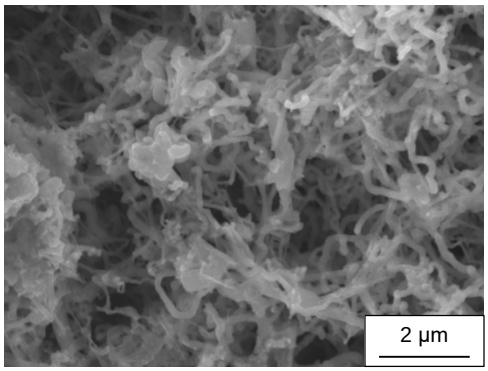

Fig. 9 FE-SEM image of the sample obtained by potentiostatic electrolysis of simulant 3 at 0.6 V for 1 h at 1103 K and washing by 3 mol/L HCl solution.

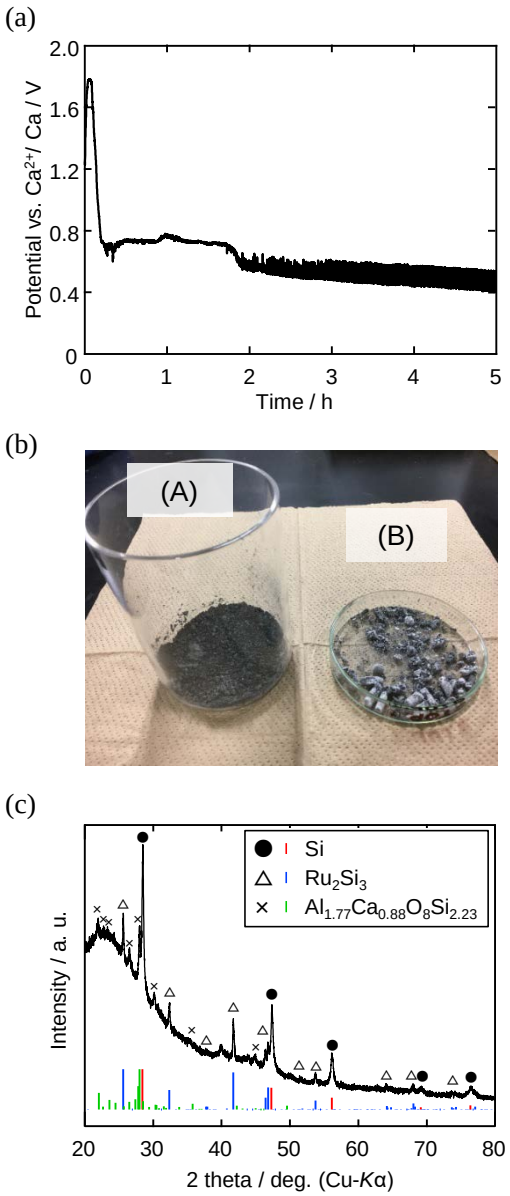

Fig. 10 (a) Potential transient curve during electrolysis in Exp. 2. (b) Photograph of the reduction products obtained by galvanostatic electrolysis of simulant 3 at −2 A for 5 h. Separated products of (A) black power and (B) the remainder with white cylindrical lumps. (c) XRD pattern for the reduction product (A).

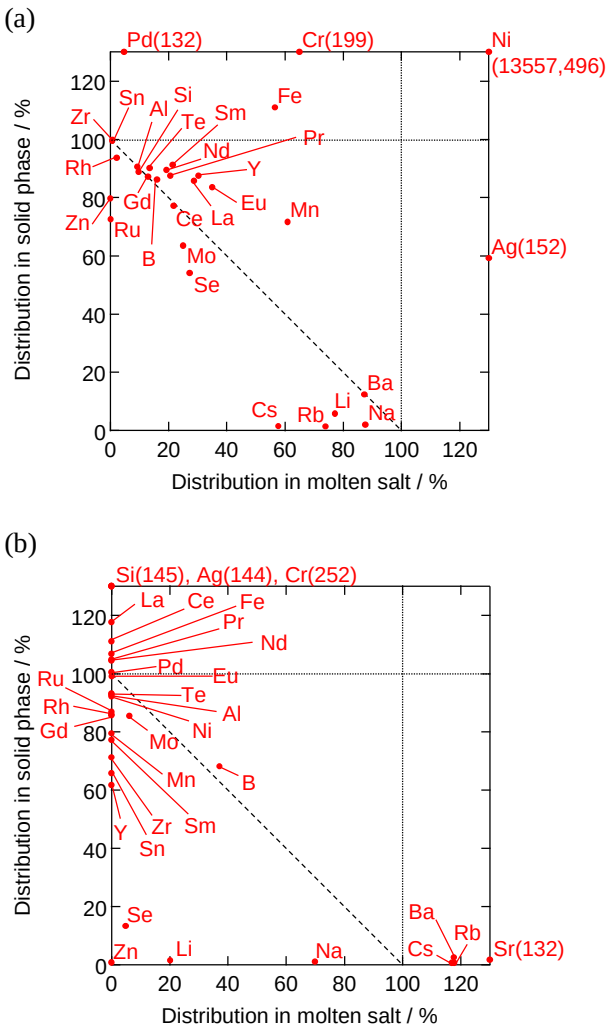

Fig. 11 Distribution of elements in molten salt and solid phase in (a) Exp. 1 and (b) Exp. 2.